12-1998

A Methodology for Acoustic Measurement and Separation of Background Noise

Sekhar Radhakrishnan
University of Tennessee - Knoxville

To the Graduate Council:

I am submitting herewith a thesis written by Sekhar Radhakrishnan entitled "A Methodology for Acoustic Measurement and Separation of Background Noise." I have examined the final electronic copy of this thesis for form and content and recommend that it be accepted in partial fulfillment of the requirements for the degree of Master of Science, with a major in Aerospace Engineering.

Ahmad D. Vakili, Major Professor

We have read this thesis and recommend its acceptance:

Charles Merkle, Ching-Fang Lo

Accepted for the Council:
Carolyn R. Hodges

Vice Provost and Dean of the Graduate School

(Original signatures are on file with official student records.)

To the Graduate Council:

I am submitting herewith a thesis written by Sekhar Radhakrishnan entitled "A Methodology for Acoustic Measurement and Separation of Background Noise." I have examined the final copy of this thesis for form and content and recommend that it be accepted in partial fulfillment of the requirements for the degree of Master of Science, with a major in Aerospace Engineering.

Ahmad D. Vakili, Major Professor

We have read this thesis
and recommend its acceptance :

Accepted for the Council :

Associate Vice Chancellor and
Dean of the Graduate School

A METHODOLOGY FOR ACOUSTIC MEASUREMENT AND SEPARATION OF BACKGROUND NOISE

A Thesis
Presented for the
Master of Science
Degree
The University of Tennessee, Knoxville

Sekhar Radhakrishnan
December 1998

DEDICATION

This thesis is dedicated to my parents

Mr. Ramamurthy Radhakrishnan

and

Mrs. Revathi Radhakrishnan

and my beloved brother

Viju

ACKNOWLEDGEMENTS

First of all, I would like to express gratitude to my advisor, Dr. Ahmad Vakili, for his help and guidance. My thanks are due to Rickey Meeker, Jim Goodman, and Jack Frazier for their help in the laboratory. Finally, I wish to thank the remaining members of my thesis committee, Dr. Charles Merkle and Dr. Ching-Fang Lo.

ABSTRACT

An attempt is made at developing experimental methods for the acoustic measurement and separation of background noise in a wind tunnel. To this end, an array beamforming technique known as delay-and-sum beamforming is identified and tested.

The theory underlying delay-and-sum beamforming is discussed. Two linear arrays, the seven microphone linear array and the four microphone minimum redundancy array, are designed. A driver is designed based on Helmholtz resonator theory to provide a source of monochromatic sound. Also, the concept of partial coherence as applicable to the separation of background noise from signal noise is investigated.

Array beamforming results show that tests conducted with the two linear arrays in the open field provide good resolution of the sound source Direction Of Arrival (DOA) peaks from the background noise, and provide a semianechoic reference with which to compare wind tunnel results. Beamforming results obtained for the driver placed inside the wind tunnel with the tunnel running at 0, 45, and 81 ft/sec successfully resolved the DOA peaks of the driver from the background noise of the tunnel. At a tunnel velocity of 151 ft/sec, the driver signal is completely buried in the background noise of the tunnel, and beamforming was not successful in resolving the peak corresponding to the driver signal.

TABLE OF CONTENTS

LIST OF FIGURES

LIST OF TABLES

TABLE PAGE

NOMENCLATURE

A	area of Helmholtz resonator opening
c	speed of sound
d	depth dimension of driver
$\hat{e}$	steering matrix
E	cross covariance between sensor outputs
f	frequency
f_R	resonant frequency of Helmholtz resonator
$f(\vec{x},t)$	equation of the wavefield
G	array gain
G_x	two-sided autospectral density function
G_{xy}	two-sided cross spectral density function
$h_0(\tau)$	weighting function
$H_0(f)$	transfer function
l	length of the neck of Helmholtz resonator opening
M	number of sensors in array
n(t)	noise component of acoustic field
$P_{i,o}$	pressure fluctuations outside Helmholtz resonator
P_b	pressure variation inside Helmholtz resonator
$P(\hat{e})$	power output of array

r^0 distance of sound source from phase center of array

r_m distance of m^{th} array sensor from steering location

r_m^0 distance of m^{th} array sensor from sound source

R_n mean square value of noise

R_s mean square value of signal

R_x autocorrelation function

R_{xy} cross correlation function

$s_p(t)$ waveform of the pth source

S^x spectral matrix of random process x(t)

S_{rs}^x one-sided spectral density of random variables r and s of random process {x(t)}

$S_{\Delta y \Delta y}$ residual spectral density function of $\Delta y(t)$

t time instant

T observation time

V volume of Helmholtz resonator

w_m amplitude weighting on the m^{th} sensor in array

x(t) random variable

$\vec{x}^0$ source location

$\vec{x}_m$ location of the mth sensor

y(t) random variable

$\hat{y}(t)$ linear prediction of y(t) from x(t)

$\Delta y(t)$ residual random variable

$z(t)$ beamformer output signal

$\vec{\alpha}^{0}$ slowness vector

γ_{xy} coherence function of random variables x(t) and y(t)

δ^{2} Kronecker delta function

Δ_{m} delay of the m^{th} array microphone

ε^{2} mean square error

λ^{0} wavelength of the propagating signal

σ^{2} variance of noise components

σ_{k}^{2} power of the k-th far-field source

ν time delay

θ_{xy} phase angle

τ time delay

ψ_{m} source direction vector

$\vec{\varsigma}^{0}$ propagation direction

Subscripts

m, n arbitrary number of the microphone, $1 \leq m,n \leq M$

Abbreviations

DOA Direction Of Arrival

MRA Minimum Redundancy Array

SNR Signal to Noise Ratio

SPL Sound Pressure Level

Chapter 1

INTRODUCTION

1.1 Statement of the Problem

Wind tunnels are notoriously difficult environments for measuring sound radiated from models. The enclosure of a model inside a wind tunnel test section (Figure 1.1) for aeroacoustic measurements can significantly change the sound field produced by the model. The hard walls of the test section reflect back some or all of the sound produced by the model. The reflected sound combines with the direct sound field in phase to increase the sound level in some regions, and out of phase to decrease the sound level in other regions. The resulting acoustic field may be very different from the direct sound field produced by the model in a free field.

Also, wind tunnels contain sources of noise such as fans, vanes and bends located outside the test section. The acoustic noise generated by the tunnel fan and/or flow disturbances outside the test section appear approximately as plane waves propagating through the test section. These plane propagating waves through the wind tunnel test section interfere with the sound field produced by the model, thus altering the sound field produced by the model. Therefore, it is desirable to separate the effects of the background tunnel noise from the model noise, in order to obtain an accurate prediction of the noise produced by the model. Cavity acoustic measurements [1] in wind tunnels

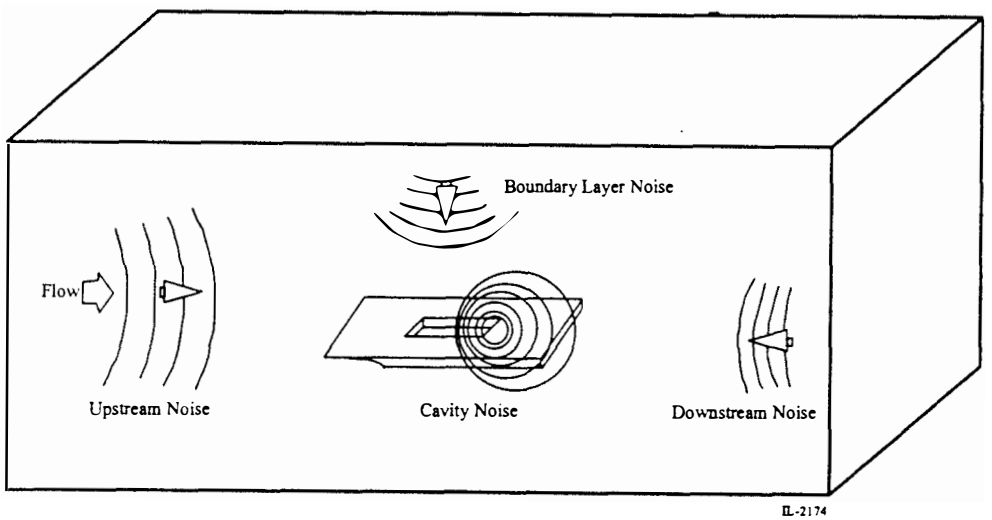

Figure 1.1 Sources of Noise in the Test Section of a Wind Tunnel

are of special interest in the application of this study.

Until recently, researchers made most acoustic measurements in wind tunnels with a single microphone or a pair of microphones. With the improved performance to cost ratio of electronic equipment and computers, it is now practical for researchers to make aeroacoustic measurements with microphone arrays, an *array* being defined as a group of sensors located in distinct spatial locations. Acoustic measurements using arrays have the following advantages over single sensor measurements.

- enhanced signal-to-noise ratio
- characterization of the field by determining the sound sources, their locations, and the waveforms they are emitting

To focus on selected signals, for instance to focus on the signal being emitted by a model placed in the test section of a wind tunnel, microphone arrays can be augmented with signal processing techniques that not only focus the array's signal-capturing abilities in a particular direction (directivity), but also allow one to focus the array in different directions without changing the physical position of the array. Beamforming is the name given to a wide variety of array processing algorithms that enhance the directivity of an array. Using beamforming algorithms to process array data, the wavefield can be decomposed into its components. Thus with array techniques, individual sources can be measured instead of the total integrated effect of all the sources of noise. In this way, the background noise of the tunnel can be separated from the acoustic signature produced by

the model.

1.2 Objective

The objective of this work is to investigate the effectiveness of two linear arrays in measuring the Sound Pressure Levels (SPL) produced by a known source of sound using an array processing algorithm called delay-and-sum beamforming. It is also desirable to develop a technique for separating the measured sound spectrum from the background noise of the wind tunnel. This work will also focus on the performance of the linear arrays in the open field which provides a semianechoic reference with which to compare the wind tunnel results. The efficiency of the two arrays with and without flow in the tunnel will be studied and compared with the open field results. The two linear arrays designed for this purpose are the seven microphone uniform linear array and the four microphone Minimum Redundancy Array (MRA).

Chapter 2

REVIEW OF LITERATURE

An extensive search was made to review methods and procedures detailed in literature which would aid in the purpose of separating wind tunnel background noise from cavity model noise. Brief reviews of papers most relevant to this work are presented below.

Piersol [2] modeled the acoustic field in the test section of a wind tunnel as a combination of diffuse noise due to the boundary layer turbulence in the test section and propagating noise generated by the tunnel fan and possible flow disturbances outside the test section. The coherence and phase measurements between two closely spaced microphones in an acoustically treated tunnel test section were predicted for various ratios of diffuse to propagating noise contributions and compared to actual measurements under several different tunnel operating conditions. The predicted values were in good agreement with the experimental results. However, the introduction of a strongly reverberant environment inside the test section resulted in a loss of accuracy.

Chung [3] developed a method for rejecting transducer flow-noise interference. The method made use of the coherence function relations between simultaneous measurements at three transducers in the signal field and extracted from the flow-noise background the power spectrum of the signal as received at each transducer. Successful

results were obtained in laboratory tests made in an anechoic chamber. The method was not so successful when there existed a large-scale eddy formation in the flow with a higher spatial correlation.

Wlezien et al. [3] decomposed the velocity fluctuations into contributions from acoustic and vortical disturbances in an effort to characterize tunnel freestream conditions. The two-point cross-coherence was developed to determine the propagation delay and direction of travel for acoustic disturbances. The two-point cross-coherence function was formed as follows. A complex-valued function was formed from the coherence and phase, and this function was inverse Fourier transformed into the time domain. The authors claimed that the temporal function so formed corresponded to the deconvolution of the cross-correlation and the respective autocorrelations, and that the contributions to the shape of the cross-correlation function from the periodic autocorrelations were removed from the peaks in the cross-correlation corresponding to the time delay between the sensors. The authors reported good separation of the acoustic noise from the vortical noise, but did not continue the work.

Shivashankara [4] used Chung's [3] three-microphone signal enhancement technique to separate aft fan , core and jet noise components of a large high bypass ratio engine (P&WA JT9D). He reported good separation results in the low-frequency limit. The engine broadband noise at higher frequencies did not satisfy the assumption required for the signal enhancement technique, that the signal due to the component of interest be well correlated between the chosen microphones. This was believed to be because the

higher frequency broadband noise sources are uncorrelated and distributed over a region of size comparable to the diameter of the engine.

Parthasarathy et al. [6] developed a method of identification and measurement of core noise and jet noise separately based on cross-correlation of signals from microphones located at widely separated angles in the far-field of the jet. The different coherent properties of core noise and jet noise were used in the method to achieve the separation. The basis of this method is as follows. Sources of core noise are nearly at rest with respect to the engine. Therefore, frequencies of the radiated core noise are preserved unchanged. However, for jet noise whose sources are in motion, the source frequencies undergo large Doppler shifts as the noise is radiated into the far field. As a consequence, the radiated field of core noise is coherent over different angular directions in contrast to jet noise which has negligible coherence over widely separated directions. Therefore, the cross-correlation between sound pressures from two microphones separated by a wide angle would essentially represent the auto-correlation of core noise radiated to the far field.

Computation of quantities such as conditioned spectral density functions, partial coherence functions, and multiple coherence functions can be used in acoustics and vibration problems to : (a) identify different multiple correlated noise sources, (b) determine multiple system frequency response functions, (c) simulate multiple random environments which preserve coherence and phase relationships among the measured points [7].

For stationary, random, or transient data representing multicorrelated (multicoherent) input/output data occurring in physical systems, Bendat [8] developed iterative computational algorithms to identify the frequency response functions of optimum constant parameter linear systems connecting this data.

Howlett [9] described results of an effort to develop partial coherence techniques for interior noise source/path determination in the highly coherent environment of a propeller-driven general aviation aircraft. Chung et al. [10] established a structural-acoustical system to model theoretically the noise generation of a six-cylinder diesel engine. In this system, the six cylinder pressures were treated as six mutually correlated inputs. The noise measured 3 ft away from the engine was treated as the single output of the system. The multiple coherence function between all the inputs and the single output was evaluated experimentally. Using the multiple coherence function, the engine noise which is coherent to the cylinder pressures was separated from the total engine noise.

Koss and Alfredson [11] located the position of sources of transient sound on a four ton punch press through the use of multiple input correlation theory. The inputs were accelerations measured at different points on the body of the press and the output was the measured sound pressure. The method of least squares fitting sound frequency data to acceleration frequency data was successfully used to locate transient sound sources on the punch press.

As mentioned before, wind tunnels are notoriously difficult environments for measuring sound radiating from models. Background noise interferes with the measurement and can exceed some noise sources of interest in any wind tunnel.

measurement and can exceed some noise sources of interest in any wind tunnel. Reflections off hard walls in closed test section wind tunnels interfere with all but extremely close near field measurements or measurements of highly directional and impulsive sources such as helicopter blade vortex interaction. With array techniques, individual sources can be measured instead of the total integrated effect of all noise sources.

Soderman and Noble [12] tested an in-flow, linear array in Ames' 40- by 80- Foot Wind Tunnel with hard walls in the early 1970's. With a time delay technique, they reported good rejection of reverberant noise at low frequencies, but did not continue the work. Grosche, Siewitt and Binder [13] investigated the potential of the acoustic mirror as a highly directional microphone system for sound source localization and discrimination from background noise, through measurements of the noise of a model source in the open test section of a low-speed wind tunnel, the mirror being positioned outside the flow. The acoustic performance of the mirror was affected by the scattering and refraction of the sound waves in the free shear layer of the tunnel, but these effects were found to be important only at high frequencies, where they approximately compensate the increase of both the spatial resolution and gain factor of the mirror with frequency.

Billingsley and Kinns [14] used the acoustic mirror technique to localize the sound sources on a Rolls-Royce/SNECMA Olympus engine. Brooks et al. [15] used a two-dimensional array in the DNW with the open jet in anechoic chamber configuration to measure noise from a model-scale helicopter. Fourier components from the

microphones were summed with appropriate phase delay and the results averaged to locate sources of noise on a model-scale helicopter. The processing included the effects of open-jet shear layer refractions in determining the correct phase delay for each microphone.

Elias [16] reports work with a linear array antenna using frequency domain beam forming with the cross spectral matrix to localize acoustic sources. Gramann and Mocio [17] report measurements of a speaker from a linear array in a hard walled wind tunnel. They processed measurements in the frequency domain with conventional beamforming with spatial shading and adaptive beamforming. Microphones were held by separate struts mounted streamwise in the wind tunnel. Tonal noise sources were played through a speaker. They located the source angle and claimed to measure the correct source amplitude to within about 2 dB.

Dougherty and Underbrink [18] designed two-dimensional array patterns to yield useful results over a wide frequency range. Using these arrays, they tested many real aeroacoustic sources using conventional beamforming for quantitative results and the MUSIC algorithm for precise source location.

Herkes and Stoker [19] used a phased microphone array in the Boeing Low-Speed Aeroacoustic facility to conduct a model-scale airframe noise test of a high-speed civil transport (HSCT) aircraft. The test had the following objectives : 1) provide an estimate of HSCT airframe noise levels; 2) identify the major airframe noise sources; and 3) assess the accuracy of the current HSCT noise predictions. A total of 103 microphones were used in the phased array data acquisition. The microphones were split into two arrays, a

low-frequency array (for frequencies upto 12 kHz) and a high-frequency array (for frequencies greater than 12 kHz). The array design for both arrays was a 7-arm logarithmic spiral pattern developed by Dougherty and Underbrink [18]. The major noise sources were identified as the wing tips, the landing gear, and the nacelle inlets.

Humphreys et al. [20] constructed a Large Aperture Directional Array (LADA) to obtain high resolution noise localization maps. A Small Aperture Directional Array (SADA) was also made to be moved about the model to provide localized spectra and directivity from selected noise source regions. The authors reported successful measurement of the far-field acoustics on a main element / half-span flap model using the two arrays. The LADA was used to detect small changes in location of dominant noise sources emanating from the flap edge region, while the SADA provided spectra and directivity measurements from this region.

Bai and Lee [21] used linear microphone arrays and beamforming algorithms like Conventional Beamforming, Minimum Variance method, and the Multiple Signal Classification method to develop a noise source identification technique for industrial applications.

Chapter 3

THEORY

There are many physical phenomena in practice which produce data that can be represented with reasonable accuracy by explicit mathematical relationships. Such phenomena are termed deterministic. However, there are many other physical phenomena which produce data that are not deterministic. For example, the height of waves in a confused sea, the acoustic pressures generated by air rushing through a pipe, or the electrical output of a noise generator represent data which cannot be described by explicit mathematical relationships. There is no way to predict an exact value at a future instant of time. These data are random in character and must be described in terms of probability statements and statistical averages rather than explicit equations [22].

Four main types of statistical functions are used to describe the basic properties of random data :

- **Mean Square Values**
- **Probability Density Functions**
- **Correlation Functions**
- **Power Spectral Density Functions**

Out of the four categories of statistical functions mentioned above, only the last two categories of statistical functions are discussed below, because they are more

germane to this work. The following sections contain a brief description of the Auto-Correlation function and the Cross-Correlation function which come under the heading of "Correlation Functions", and a description of the Auto-Spectral density function and the Cross-Spectral density function which are categorized under "Power Spectral Density Functions".

3.1 Correlation Functions

3.1.1 Auto-Correlation Function

The *Auto-Correlation* function of random data describes the general dependence of the values of the data at one time on the values at another time. Consider the sample time history record *x(t)* shown in Figure 3.1. An estimate for the auto-correlation function between the values of t and $t+\tau$ may be obtained by taking the product of the two values and averaging over the observation time T. The resulting average product will approach an exact auto-correlation function as T approaches infinity. In equation form,

$$R_x(\tau) = \lim_{T\to\infty} \frac{1}{T} \int_0^T x(t)x(t+\tau)dt \tag{3.1}$$

The quantity $R_X(\tau)$ is always real-valued even function with a maximum at $\tau = 0$, and may be either positive or negative. In equation form,

$$\begin{aligned} R_x(-\tau) &= R_x(\tau) \\ R_x(0) &\geq \left|R_x(\tau)\right| \end{aligned} \tag{3.2}$$

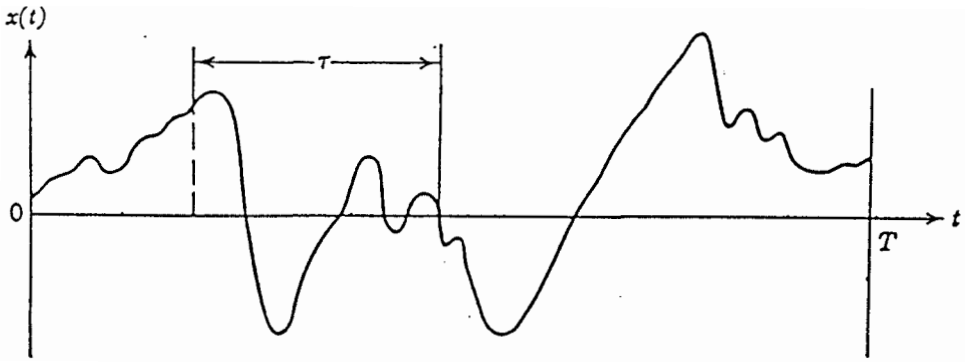

Figure 3.1 Autocorrelation Measurement [22]

Consider the four special time histories shown in Figure 3.2. Auto-Correlation function plots (autocorrelograms) for these time histories is shown in Figure 3.3.

The principal application for an Auto-Correlation function measurement of physical data is to establish the influence of values at a future time. Because a Sine wave, or any other deterministic data, will have an Auto-Correlation function which persists over all the displacements, an Auto-Correlation measurement clearly provides a tool for detecting deterministic data which might be masked in a random background.

3.1.2 Cross-Correlation Function

The Cross-Correlation function of two sets of random data describes the general dependence of the values of one set of data on the other. Consider the pair of time history records $x(t)$ and $y(t)$ illustrated in Figure 3.4. An estimate of the Cross-Correlation function of the values of $x(t)$ at time t and $y(t)$ at time $t+\tau$ may be obtained by taking the average product of the two values over the observation time T. The resulting average product will result in an exact Cross-Correlation function as T approaches infinity, i.e.,

$$R_{xy}(\tau) = \lim_{T\to\infty} \frac{1}{T} \int_0^T x(t)y(t+\tau)dt \tag{3.3}$$

The function $R_{xy}(\tau)$ is always a real-valued function, which may either be positive or negative. When $R_{xy}(\tau) = 0$, $x(t)$ and $y(t)$ are said to be uncorrelated. If $x(t)$ and $y(t)$ are statistically independent , then $R_{xy}(\tau) = 0$ for all time displacements. A typical Cross-Correlation plot is shown in Figure 3.5.

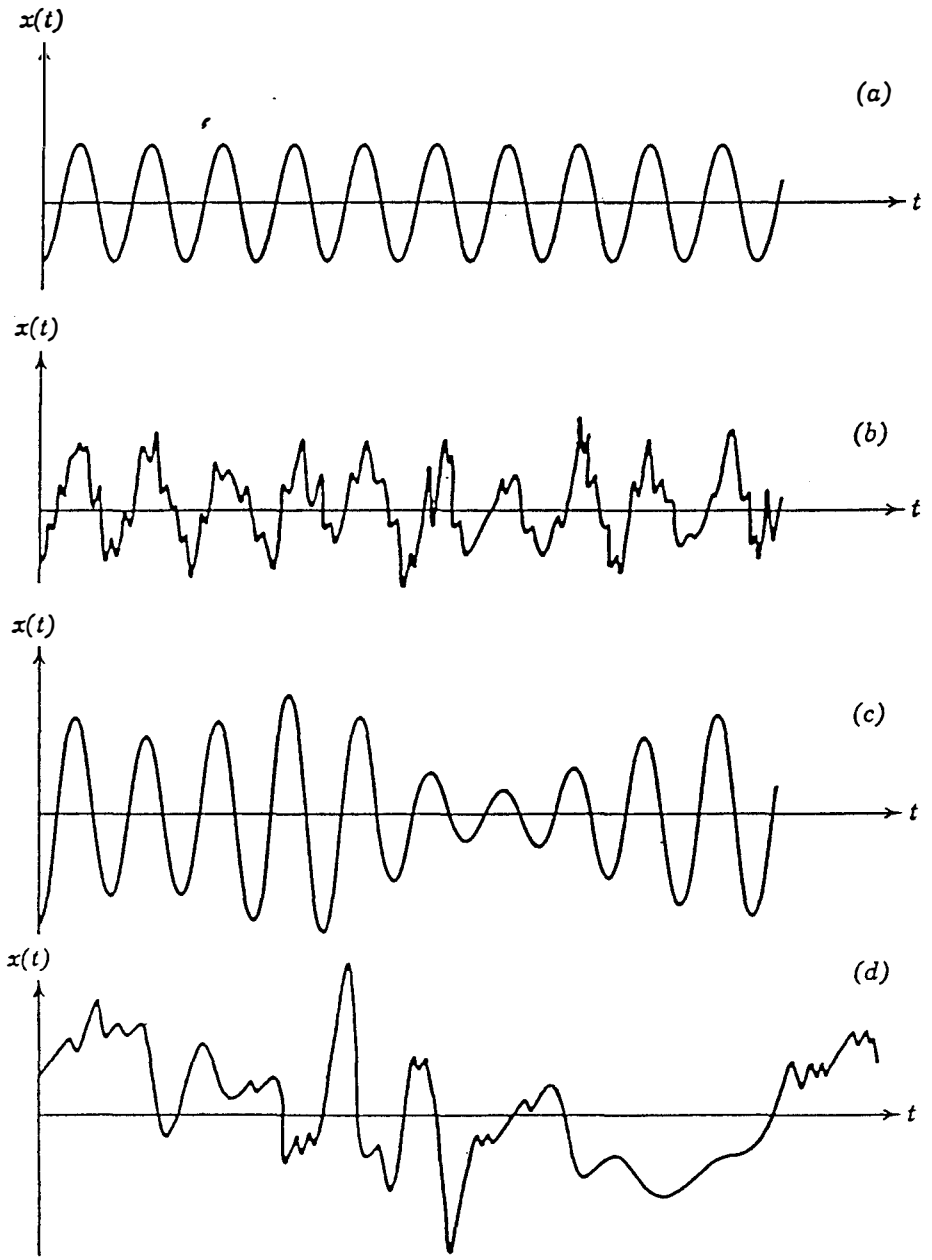

Figure 3.2 Four Special Time Histories. (a) Sine wave. (b) Sine wave plus random noise. (c) Narrow-band random noise. (d) Wide-band random noise [22]

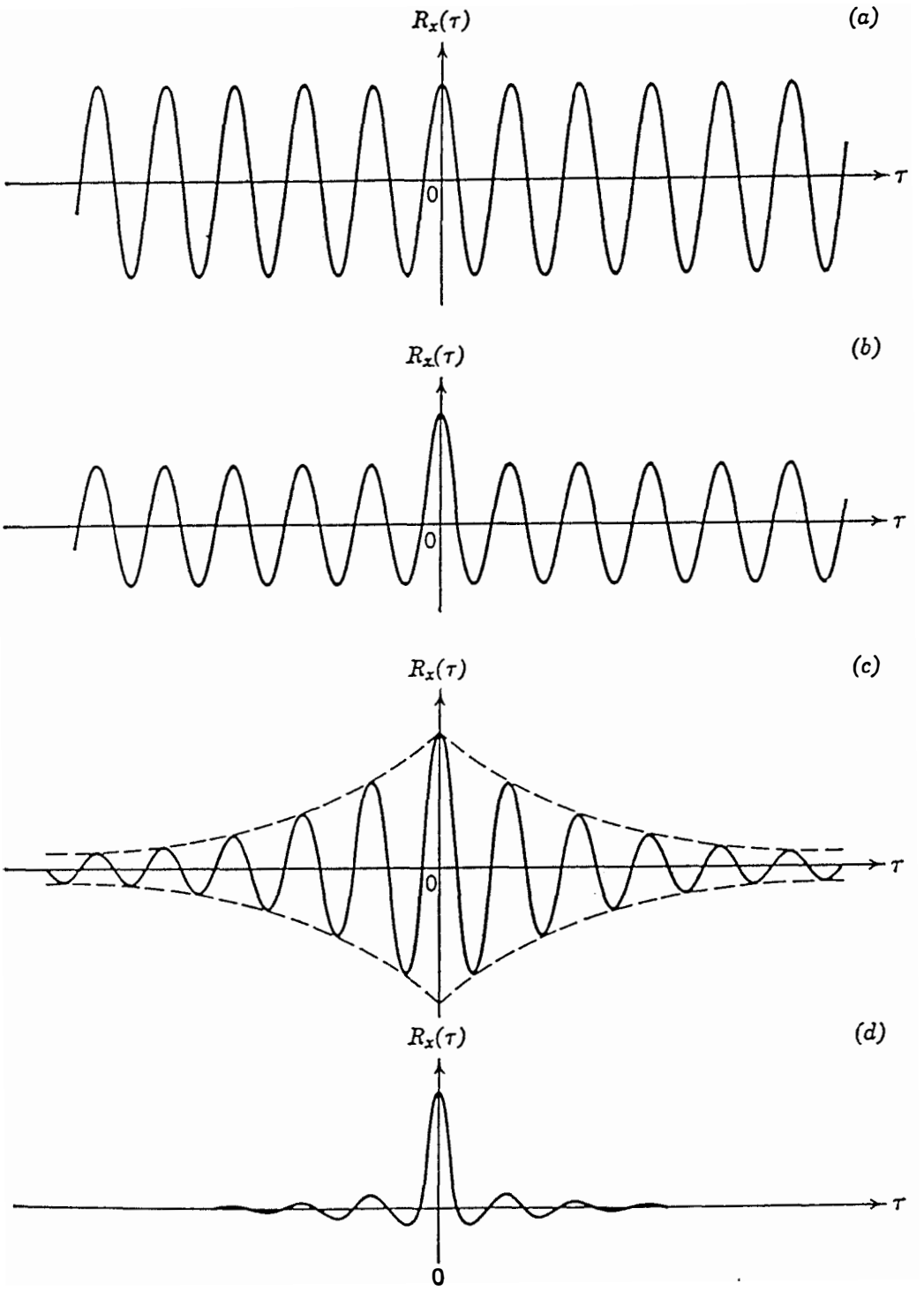

Figure 3.3 Autocorrelograms. (a) Sine wave. (b) Sine wave plus random noise. (c) Narrow-band random noise. (d) Broad-band random noise [22]

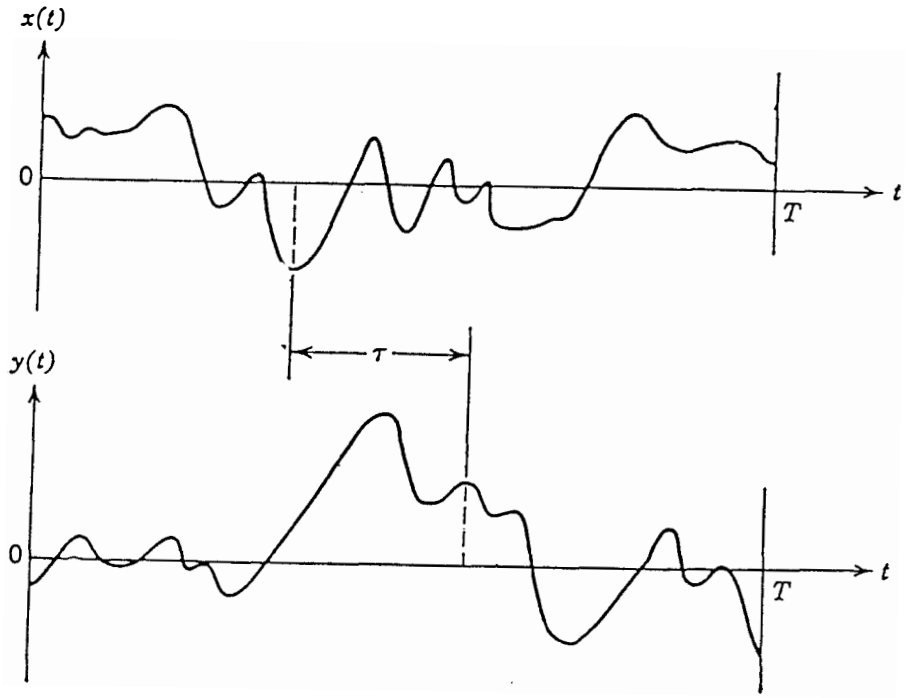

Figure 3.4 Cross-Correlation Measurement [22]

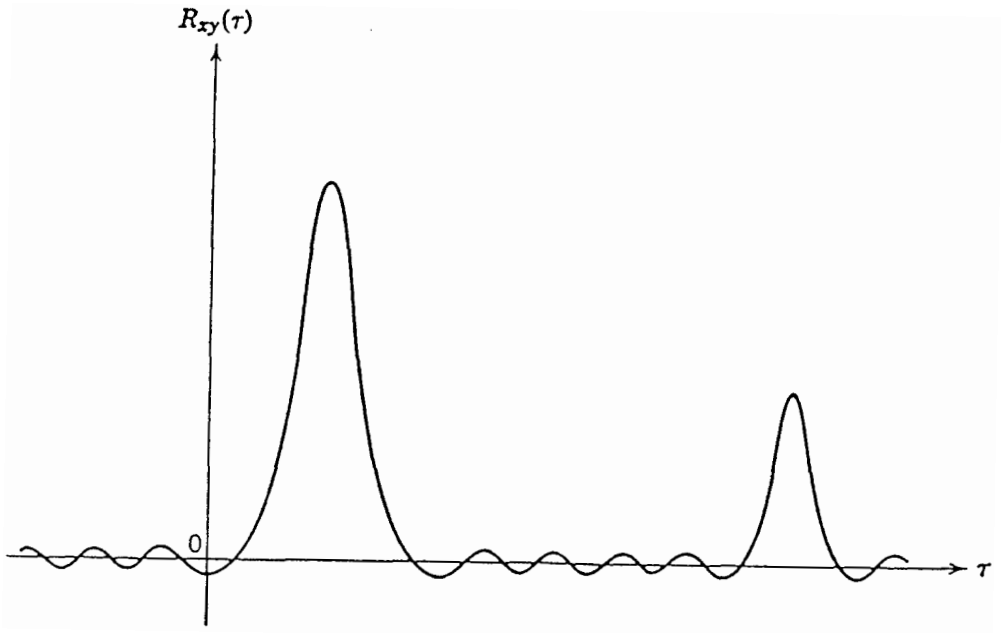

Figure 3.5 Typical Cross-correlation plot (Cross-correlogram)[22]

Cross-Correlation measurements have many important applications and some of them are discussed below.

Measurement of Time Delays : As the output from the system is displaced in time relative to the input, the Cross-Correlation function will peak at that time displacement equal to the time require for the signal to pass through the system. Hence a system time delay can be established directly by noting the time displacement associated with an observed peak in the Cross-Correlogram between the input and the output.

Determination of Transmission Paths : As every transmission path through the system is generally associated with a different delay time, a separate peak will occur in the Cross-Correlogram for each path which contributes significantly to the output. If the expected time delays associated with the various paths can be calculated, tese expected delays can then be compared to the measured time displacements of the peaks in the Cross-Correlogram to identify the paths contributing significantly to the output.

Detection and recovery of Signals in Noise : A third application for the Cross-Correlation function is the detection and recovery of a signal buried in extraneous noise, where the signal buried is not necessarily in the periodic form. If a noise-free replica of the signal (either random or periodic) which one wishes to detect is available, then a Cross-Correlation of the signal plus noise with a stored replica of the signal alone will extract the correlation function of the signal. Furthermore, for the case of periodic signals, the Cross-Correlation function will provide a greater signal-to-noise ratio than will the Auto-Correlation function for any given input signal-to-noise ratio and sample record length.

3.2 Power Spectral Density Functions

3.2.1 Auto-Spectral Density Function

The Auto-Spectral density function of random data describes the general frequency composition of the data in terms of the spectral density of its mean-square value. An important property of the Auto-Spectral density function lies in its relationship to the Auto-Correlation function. Specifically, for stationary data, the two functions are related by a Fourier transform as follows.

$$G_x(f) = 2\int_{-\infty}^{\infty} R_x(\tau)e^{-j2\pi ft}d\tau = 4\int_{0}^{\infty} R_x(\tau)\cos(2\pi ft)d\tau \qquad (3.4)$$

The second equality exists because $R_X(\tau)$ is an even function of τ. A typical plot of Auto-Spectral Density versus frequency [$G_X(f)$ versus f] for each of the time histories shown in Figure 3.2 is presented in Figure 3.6. these plots are called *Power Spectra.*

The principal application for an Auto-Spectral density measurement of physical data is to establish the frequency composition of the data, which in turn, bears important relationships to the basic characteristics of the system involved. However, Auto-Spectral densities of physical data yield information only about the amplitude of the signal. Determination of phase information requires a Cross-Spectra analysis which is described in the next section.

3.2.2 Cross-Spectral Density Function

The Cross-Spectral density function of a pair of time history records is the Fourier transform of the Cross-Correlation function of the pair of time history records. Since the

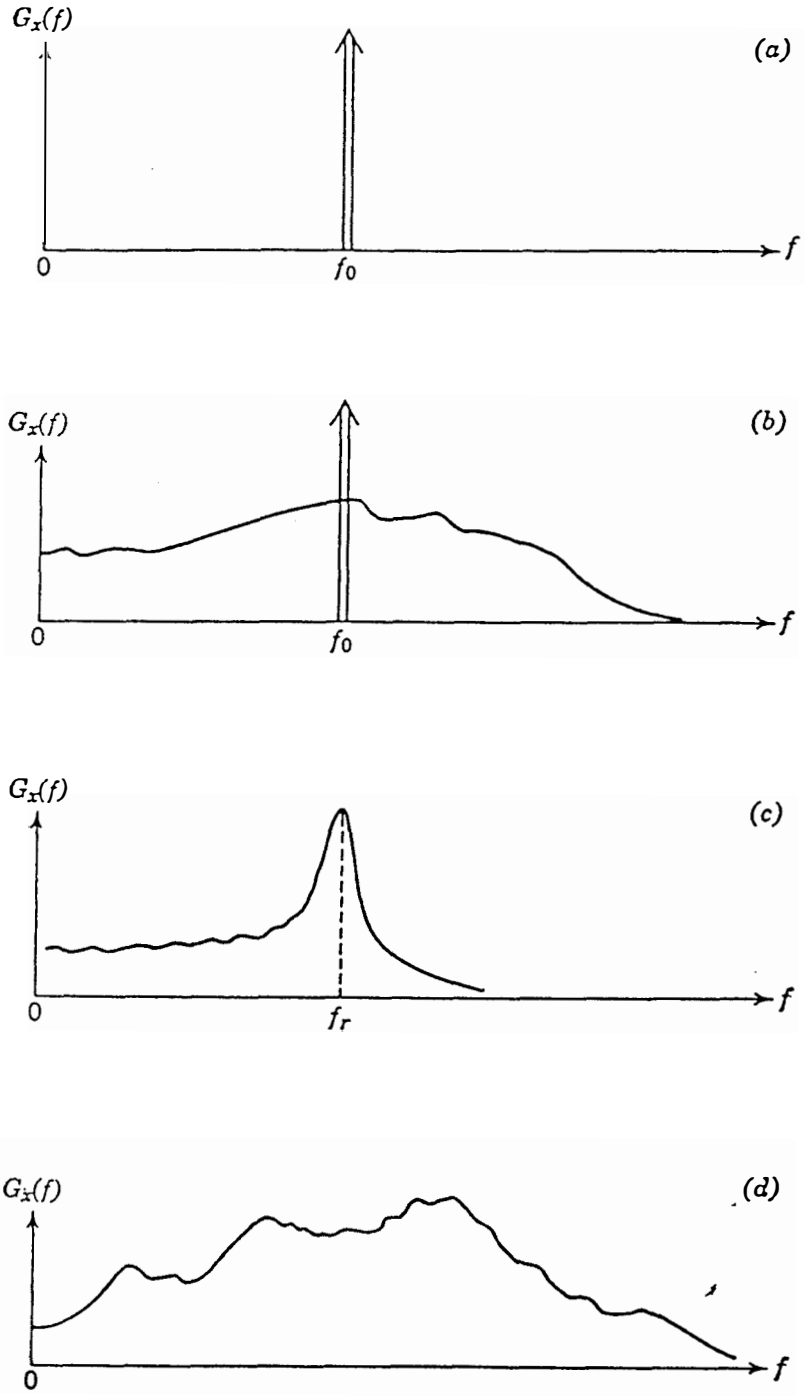

Figure 3.6 Autospectral Density Plots (Power-Spectra). (a) Sine wave. (b)Sine wave plus Random noise. (c) Narrow-band Random Noise. (d) Broad-band Random Noise. [22]

Cross-Correlation function is not an even function, the Cross-Spectral density is generally a complex number such that

$$G_{xy}(f) = C_{xy}(f) - jQ_{xy}(f) \tag{3.5}$$

where the real part, $C_{xy}(f)$, is called the *coincident spectral density function,* and the imaginary part, $Q_{xy}(f)$, is called the *quadrature spectral density function.* It is convenient to express the Cross-Spectral density function in complex polar notation such that

$$G_{xy}(f) = \left|G_{xy}(f)\right| e^{-j\theta_{xy}(f)} \tag{3.6}$$

where

$$\left|G_{xy}(f)\right| = (C_{xy}^2(f) + Q_{xy}^2(f))^{\frac{1}{2}} \qquad \text{and}$$

$$\theta_{xy}(f) = \tan^{-1}\left[\frac{Q_{xy}(f)}{C_{xy}(f)}\right]$$

Another useful relationship is

$$\left|G_{xy}(f)\right|^2 \leq G_x(f)G_y(f) \tag{3.7}$$

When applying the Cross-Spectral density information to physical problems, it is often desirable to use a real-valued quantity given by

$$\gamma_{xy}^2(f) = \frac{\left|G_{xy}(f)\right|^2}{G_x(f)G_y(f)} \leq 1 \tag{3.8}$$

where $\gamma_{xy}^2(f)$ is called the *coherence function.* When $\gamma_{xy}^2(f) = 0$ at a particular frequency, *x(t)* and *y(t)* are said to be incoherent at that frequency, which is simply another word for uncorrelated. If *x(t)* and *y(t)* are statistically independent, then the coherence function is zero for all frequencies. When the coherence function is equal to *1* for all frequencies, then *x(t)* and *y(t)* are said to be fully coherent.

A typical plot of the Cross-Spectral density function versus frequency [$G_{xy}(f)$ versus *f*] for a pair of time history records is shown in Figure 3.7. This plot is called a *Cross-Spectrum*. The plot consists of two parts which give a magnitude and a phase. Cross-Spectral density function measurements have many applications similar to Cross-Correlation function measurements.

3.2.3 Partial Coherence

Coherence between any two components of a multivariate random process arises from some form of response relationship existing between them. However, the coherence function which connects a response and a *single* excitation, becomes very different when other excitations are added and so modify the response. Therefore, a technique called *partial coherence* is needed to uncover that coherence which existed between the two original components.

Consider a multivariate random process *{x(t)}*. Then the spectral matrix S^x is given by

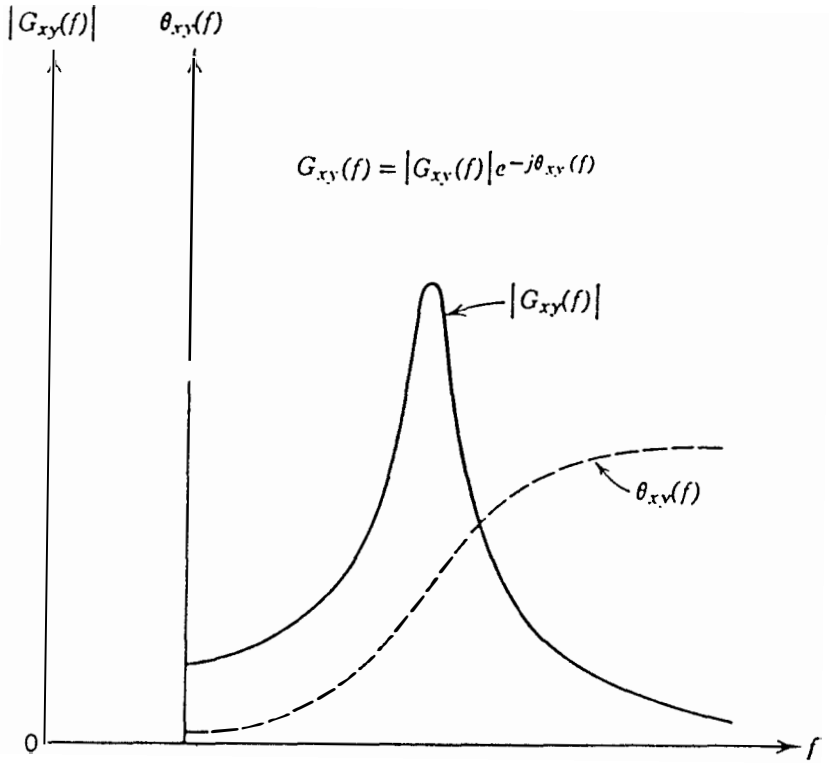

Figure 3.7 Typical Cross-Spectral Density Plot (Cross-Spectrum) [22]

$$S^x = \begin{bmatrix} S_{11}^x & S_{12}^x & \cdots & S_{1n}^x \\ S_{21}^x & S_{22}^x & \cdots & S_{2n}^x \\ \vdots & & & \\ S_{n1}^x & S_{n2}^x & \cdots & S_{nn}^x \end{bmatrix} \tag{3.9}$$

The above matrix is Hermitian

$$\Rightarrow S_{ij}^x = S_{ji}^{x^*}$$

where $S_{ji}^{x^*}$ is the complex conjugate of S_{ji}^x

The coherence function is defined by

$$\gamma_{rs}^{x\,2} = \frac{S_{rs}^x S_{sr}^x}{S_{rr}^x S_{ss}^x} \tag{3.10}$$

Define $$\gamma^x = \begin{bmatrix} \gamma_{11}^x & \gamma_{12}^x & \cdots & \gamma_{1n}^x \\ \vdots & & & \\ \gamma_{n1}^x & \gamma_{n2}^x & \cdots & \gamma_{nn}^x \end{bmatrix} \tag{3.11}$$

It is known that if $x_r(t)$ and $x_s(t)$ are fully coherent, then the r^{th} and s^{th} rows are linearly proportional,

$$\frac{S_{r1}}{S_{s1}} = \frac{S_{r2}}{S_{s2}} = \cdots = \frac{S_{rn}}{S_{sn}} \tag{3.12}$$

The γ^x matrix is such that

$$\gamma_{sr} = \gamma_{rs} = 1 \text{ and } \gamma_{1r} = \gamma_{1s},\ \gamma_{2r} = \gamma_{2s},\ \ldots,\ \gamma_{nr} = \gamma_{ns} \tag{3.13}$$

3.2.3.1 Residual Random Variables

Consider any two real-valued stationary random processes {x(t)} and {y(t)}. A linear prediction $\hat{y}(t)$ of y(t) from x(t) can be described by the following equation

$$\hat{y}(t) = \int_0^\infty h_0(\tau)x(t-\tau)d\tau \tag{3.14}$$

Here $h_0(\tau)$ is a weighting function to be determined. $h_0(\tau)$ is chosen such that the mean square error ε^2 given by

$$\varepsilon^2 = E\left[\left\{y(t)-\hat{y}(t)\right\}^2\right] = E\left[\left\{y(t)-\int_0^\infty h_0(\tau)x(t-\tau)d\tau\right\}^2\right] \tag{3.15}$$

$$= R_{yy}(0) - 2\int_0^\infty h_0(\tau)R_{xy}(\tau)d\tau + \int_0^\infty\int_0^\infty h_0(\tau)h_0(\nu)R_{xx}(\tau-\nu)d\nu d\tau \tag{3.16}$$

is a minimum over all possible choices of $h_0(\tau)$. This condition is satisfied by that $h_0(\tau)$ which makes

$$\frac{\partial\varepsilon^2}{\partial h_0(\tau)} = 0 \tag{3.17}$$

This leads to the convolution integral result,

$$R_{xy}(\tau) = \int_0^\infty h_0(\nu)R_{xx}(\tau-\nu)d\nu \tag{3.18}$$

which, upon taking Fourier transforms on both sides, is equivalent to

$$S_{xy}(f) = H_0(f)S_{xx}(f) \tag{3.19}$$

The *residual random variable* $\Delta y(t)$ resulting from y(t), is denoted by

$$\Delta y(t) = y(t) - \int_0^\infty h_0(\tau)x(t-\tau)d\tau \tag{3.20}$$

Then the autocorrelation function $R_{\Delta y \Delta y}$ is given by

$$R_{\Delta y \Delta y}(\tau) = R_{yy}(\tau) - \int_0^\infty h_0(\nu)R_{yx}(\tau-\nu)d\nu \tag{3.21}$$

The Fourier transform of equation (3.21) leads to

$$S_{\Delta y \Delta y}(f) = S_{yy}(f) - H_0(f)S_{yx}(f) \tag{3.22}$$

Use of equation (3.19) then gives

$$S_{\Delta y \Delta y}(f) = S_{yy}(f) - \frac{S_{xy}(f)S_{yx}(f)}{S_{xx}(f)} \tag{3.23}$$

$$= S_{yy}(f)\left[1 - \gamma_{xy}^2(f)\right] \tag{3.24}$$

where

$$\gamma_{xy}^2(f) = \frac{\left|S_{xy}(f)\right|^2}{S_{xx}(f)S_{yy}(f)} \tag{3.25}$$

is the ordinary coherence function between x and y. The quantity $S_{\Delta y \Delta y}(f)$ is called the *residual spectral density function* of $\Delta y(t)$.

3.2.3.2 First Order Partial Coherence

Consider the multivariate random process [23], e.g. to establish spectral properties of x_2 and x_3 after removing x_1. Defining

$$
\begin{aligned}
x_1(t) &= y_1(t) \\
x_2(t) &= y_2(t) + y_3(t) \\
x_3(t) &= y_4(t) + y_5(t)
\end{aligned}
\tag{3.26}
$$

such that $y_2(t)$ and $y_4(t)$ are fully coherent to $y_1(t)$ (i.e. to $x_1(t)$) and $y_3(t)$ and $y_5(t)$ are uncoherent with $y_1(t)$.

$$
\begin{aligned}
\therefore\ & S_{11}^x = S_{11}^y, S_{12}^x = S_{12}^y + S_{13}^y \\
& S_{13}^x = S_{14}^y + S_{15}^y, S_{22}^x = S_{22}^y + S_{23}^y + S_{32}^y + S_{33}^y \\
& S_{23}^x = S_{24}^y + S_{25}^y + S_{34}^y + S_{35}^y, S_{33}^y = S_{44}^y + S_{45}^y + S_{54}^y + S_{55}^y
\end{aligned}
\tag{3.27}
$$

Now the coherence relations are

$$
\frac{S_{21}}{S_{11}} = \frac{S_{22}}{S_{12}} = \frac{S_{23}}{S_{13}} = \frac{S_{24}}{S_{14}} = \frac{S_{25}}{S_{15}}; \frac{S_{41}}{S_{11}} = \frac{S_{42}}{S_{12}} = \frac{S_{43}}{S_{13}} = \frac{S_{44}}{S_{14}} = \frac{S_{45}}{S_{15}} \tag{3.28}
$$

and from the lack of coherence

$$
S_{13}^y = S_{31}^y = S_{15}^y = S_{51}^y = 0 \tag{3.29}
$$

Solving (3.27), (3.28) and (3.29) for S^y we get,

$$S^{y} = \begin{bmatrix} S_{11}^{x} & S_{12}^{x} & 0 & S_{13}^{x} & 0 \\ S_{21}^{x} & \left(\gamma_{12}^{x}\right)^2 S_{22}^{x} & 0 & \dfrac{S_{13}^{x} S_{21}^{x}}{S_{11}^{x}} & 0 \\ 0 & 0 & S_{22}^{x}\left[\left(1-\gamma_{12}^{x}\right)^2\right] & 0 & S_{23}^{x} - \dfrac{S_{13}^{x} S_{21}^{x}}{S_{11}^{x}} \\ S_{31}^{x} & \dfrac{S_{31}^{x} S_{12}^{x}}{S_{11}^{x}} & 0 & \left(\gamma_{13}^{x}\right)^2 S_{33}^{x} & 0 \\ 0 & 0 & S_{32}^{x} - \dfrac{S_{31}^{x} S_{12}^{x}}{S_{11}^{x}} & 0 & S_{33}^{x}\left[1-\left(\gamma_{13}^{x}\right)^2\right] \end{bmatrix}$$

$$S_{35}^{y} = S_{23}^{x} - \frac{S_{21}^{x} S_{13}^{x}}{S_{11}^{x}}$$

(3.30)

S_{35}^{y} is called the *residual cross-spectral density* of $x_2(t)$ and $x_3(t)$ with respect to $x_1(t)$, and it is conveniently denoted by $S_{23\cdot1}^{x}$. The *partial coherence* of $x_2(t)$ and $x_3(t)$ with respect to $x_1(t)$ is given by

$$\text{and} \quad \left(\gamma_{23\cdot1}^{x}\right)^2 = \frac{S_{23\cdot1}^{x} S_{32\cdot1}^{x}}{S_{22\cdot1}^{x} S_{33\cdot1}^{x}} \tag{3.31}$$

The higher order partial coherences can be computed extending the above procedure.

3.3 Arrays

Propagating signals contain much information about the sources that produce them. Not only does each waveform express the nature of the source, its temporal and spatial characteristics allow us to determine the source's location. In the real world, several sources in addition to the one of interest, and noise contaminate the desired signal.

Thus, it is desirable to *focus* on selected signals. An *array* of sensors, which is a geometrical arrangement of sensors in space, can be used to focus on the selected signal instead of using a single sensor, because of the following reasons.

- The array's output has a higher signal-to-noise ratio than that of a single sensor's output.
- The array can be used for determining the number of sources of propagating energy, and the location of these sources due to the array's directivity characteristics unlike the single sensor which is omnidirectional.

Augmenting an array with signal processing techniques can enhance directivity and can be used to aim the array's directivity pattern without physically moving the array. *Beamforming* is the name given to a wide variety of array processing algorithms that focus the array's signal-capturing abilities in a particular direction. One such beamforming technique called the *Delay-and-Sum* technique is described below.

3.3.1 Delay-and-Sum Beamforming

The idea on which the Delay-and-Sum Beamforming technique is based is the following [24]: If a propagating signal is present in an array's aperture, the sensor outputs, delayed by appropriate amounts and added together, reinforce the propagating signal with respect to noise or waves propagating in different directions. The delays that reinforce the signal are directly related to the length of time it takes for the signal to propagate between sensors.

Consider Figure 3.8. Let *s(t)* denote the signal emanating from a source located at the point $\vec{x}^{\,0}$. Several sources may be present, and their radiations sum to comprise the wavefield $f(\vec{x},t)$ measured by the sensors. Let's consider an array of M sensors located at $\{\vec{x}_m\}$, $m = 0, \ldots, M-1$. The *phase center* of the array is defined as the vector quantity $\sum \vec{x}_m$. For convenience, we choose the origin of the coordinate system to coincide with the phase centre, i.e.,

$$\sum_{m=0}^{M-1} \vec{x}_m = \vec{0} \tag{3.32}$$

The waveform measured by the m th sensor is given by $y_m(t) = f(\vec{x}_m,t)$; the sensor samples the wavefield spatially at the sensor's location. The delay-and-sum beamformer consists of applying a delay Δ_m and an amplitude weight w_m to the output of each sensor, then summing the resulting signals as shown in Figure 3.9. We define the delay-and-sum beamformer's output signal to be

$$z(t) = \sum_{m=0}^{M-1} w_m y_m(t - \Delta_m) \tag{3.33}$$

The amplitude weighting is sometimes called the array's *shading* or *taper,* and, enhances the beam's shape and reduces sidelobe levels. The delays are adjusted to focus the array's beam on signals propagating in a particular direction $\vec{\zeta}^{\,0}$ or from a particular point $\vec{x}^{\,0}$ in space.

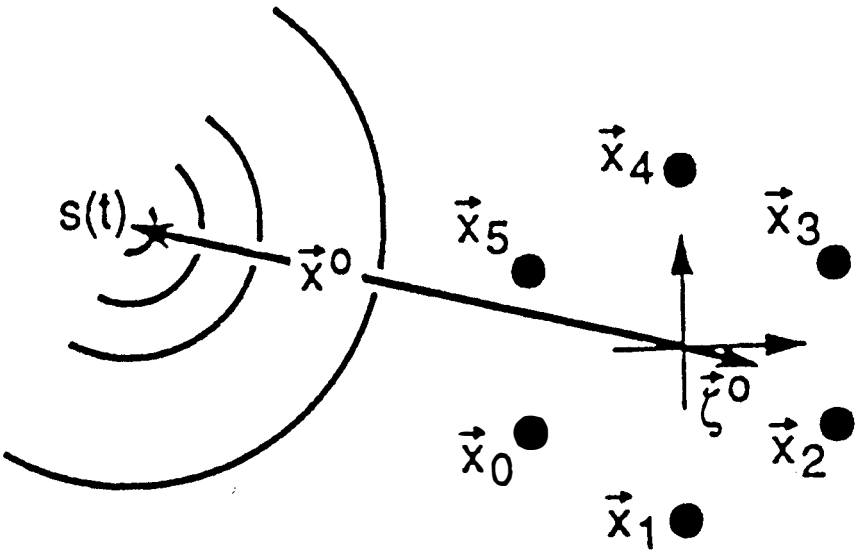

Figure 3.8 Array Coordinate system [24]

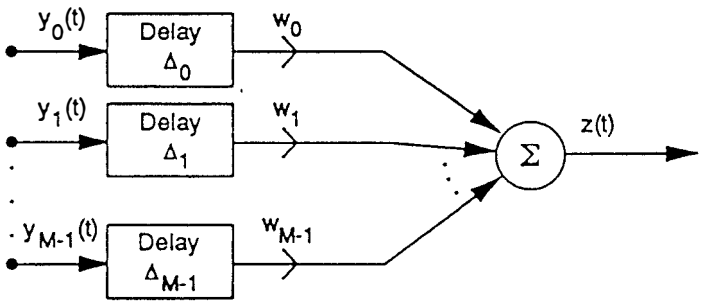

Figure 3.9 Delay-and-Sum Beamforming [24]

3.3.2 Near-Field and Far-Field Sources

Beamforming algorithms vary according to whether the sources are located in the *near field* or in the *far field*. If the source is close to an array - in the near field- the wavefront of the propagating wave is curved with respect to the dimensions of the array and the wave propagation direction depends on sensor location. If the direction of propagation is approximately equal at each sensor, then the source is located in the array's far field and the propagating field within the array aperture consists of plane waves.

A particular signal's direction of propagation relative to the coordinate system as shown in Figure 3.10 (a) is denoted by $\vec{\zeta}^0$. For plane waves, this vector does not vary with sensor location. For near-field sources, however, the apparent direction of propagation varies across the array.

To estimate the errors induced by assuming far-field propagation instead of near-field, let ε_m be the angle between the rays emanating from the source to the array origin and to the mth sensor as shown in Figure 3.10 (b). This angle represents the error we want to estimate. An application of the Law of Sines yields $\sin(\varepsilon_m) = \sin(\psi_m).(|\vec{x}_m| / r_m^0)$, with ψ_m denoting the angle between the vectors $\vec{x}_m$ and $\vec{x}^0$. When $r_m^0 >> |\vec{x}_m|$, the source is located well outside the array's aperture; we can make the approximation $r_m^0 \approx r^0$ and assume the angle ε_m is small.

Therefore,
$$\varepsilon_m \approx \frac{|\vec{x}_m|}{r^0} \sin\psi_m \qquad (3.34)$$

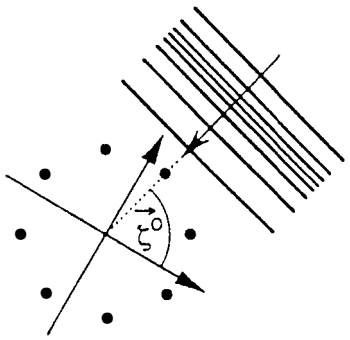

(a)

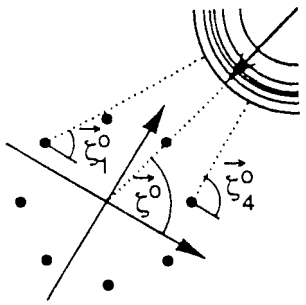

(b)

Figure 3.10 Array Geometry. (a) Far-field geometry(b) Near-field geometry [24]

The largest value of this error occurs for the most distant sensor located at a right angle relative to the source direction vector ($\psi_m = \pi/2$).

3.3.3 Beamforming for Plane Waves

A judicious choice of sensor delays $\{\Delta_m\}$ in the delay-and-sum beamformer allows the array to "look" for signals propagating in a particular direction. By adjusting the delays, the array's direction of look can be steered toward the source of radiation. Define an assumed propagation direction, denoted by the unit vector $\vec{\zeta}$. Assume a far-field source radiates a plane wave having waveform *s(t)* that propagates across an array of *M* sensors in the direction $\vec{\zeta}^0$. The wavefield within the array's aperture is expressed by

$$f(\vec{x},t) = s(t - \vec{\alpha}^0 \cdot \vec{x}) \tag{3.35}$$

where the slowness vector is defined by $\vec{\alpha}^0 = \frac{\vec{\zeta}^0}{c}$. The *m*th sensor spatially samples the wavefield, yielding $y_m(t) = s(t - \vec{\alpha}^0 \cdot \vec{x}_m)$; the delay-and-sum beamformer's output signal becomes

$$z(t) = \sum_{m=0}^{M-1} w_m s(t - \Delta_m - \vec{\alpha}^0 \cdot \vec{x}_m) \tag{3.36}$$

If we choose

$$\Delta_m = -\vec{\alpha}^0 \cdot \vec{x}_m = \frac{-\vec{\zeta}^0 \cdot \vec{x}_m}{c} \tag{3.37}$$

the signal processing delays compensate for the propagation delays and the waveforms captured by the individual sensors add constructively. In this case, the array's output equals

$$z(t) = s(t) \cdot \left[\sum_{m=0}^{M-1} w_m \right] \tag{3.38}$$

and the beamformer's signal equals a constant times the waveform radiated by the source. We can thus steer the array's beam to an assumed propagation direction $\vec{\zeta}$ by using the set of delays given by

$$\Delta_m = \frac{-\vec{\zeta} \cdot \vec{x}_m}{c} = -\vec{\alpha} \cdot \vec{x}_m \tag{3.39}$$

The beamformer signal *z(t)* that results from a plane wave propagating in the direction $\vec{\zeta}^0$ is given by

$$z(t) = \sum_{m=0}^{M-1} w_m s(t + (\vec{\alpha} - \vec{\alpha}^0) \cdot \vec{x}_m) \tag{3.40}$$

If we look in the wrong direction $\vec{\alpha} \neq \vec{\alpha}^0$, we obtain a degraded version of the propagating signal. In such cases, we say that the beamformer is *mismatched* to the propagating wave. This mismatch can occur in one of two ways.

- If the speed of propagation is known, mismatch means that the assumed propagation direction does not equal the true direction of propagation. Knowing the speed of propagation implies that the medium is relatively stable and its characteristics can be predicted or measured.

- If the direction of propagation is known, we assumed the wrong speed of propagation. Precise knowledge of source locations occurs when we place them and calibrate their positions Assuming a propagation direction thus becomes equivalent to assuming a speed of propagation.

Thus, assuming a slowness vector for the delay-and-sum beamformer means that we are presuming a direction of propagation and a propagation speed. If one of these is known. we can find the other by scanning across wavenumber with a beamformer, searching for a maximum energy output.

3.3.4 Beamforming for Spherical Waves

Consider the case of a source located in the array's near field. Assume that the source is emitting a signal *s(t)* that spreads spherically into space. We know that a spherically symmetric solution to the wave equation has the form

$$f(\vec{x},t) = \frac{s(t - |\vec{x} - \vec{x}^{\bullet}| / c)}{|\vec{x} - \vec{x}^{0}|} \tag{3.41}$$

The mth sensor thus measures the signal $y_m(t) = \frac{s\left(t - \frac{r_m^0}{c}\right)}{r_m^0}$, where r_m^0 is the distance between the source and the sensor, and, as usual, c represents wave propagation speed.

By choosing

$$\Delta_m = \frac{r^0 - r_m^0}{c} \tag{3.42}$$

we can "stack" the signal replicas captured by all the M sensors so that they reinforce each other. The beamformer's response to a spherically propagating wave becomes

$$z(t) = \frac{1}{r^0} s\left(t - \frac{r^0}{c}\right)\left[\sum_{m=0}^{M-1} w_m \frac{r^0}{r_m^0}\right] \tag{3.43}$$

The source signal emerges, delayed and attenuated as if it had been received at phase center, times a weighting factor that, for large values of r°, approaches the sum of the sensor weights. Let r and r_m denote range parameters presumed by the beamformer that do not equal actual values. The beamformer's output in this case becomes

$$z(t) = \sum_{m=0}^{M-1} \frac{w_m}{r_m^0} s\left(t - \frac{r - (r_m^0 - r_m)}{c}\right) \tag{3.44}$$

3.3.5 Array Gain

Array gain measures an array's signal-to-noise ratio enhancement and concisely summarizes how well the array and subsequent signal processing reject noise.

If a single sensor were located at the spatial origin, its response to a noise-corrupted signal would be

$$y(t) = s(\vec{0}, t) + n(\vec{0}, t) \tag{3.45}$$

where $n(\vec{x}, t)$ represents the noise field. This noise may be attributed to the sensor or to background radiation. For simplicity, assume that the desired signal is a wideband plane

wave of the form $s(\vec{x},t) = s(t - \vec{\alpha}^0 \cdot \vec{x})$, which means that a single sensor's output signal is $s(t) + n(\vec{0},t)$. Assume that s and n are stationary random fields and are uncorrelated. The signal-to-noise ratio *SNR* is defined to be the ratio of the mean-squared values of the signal and noise components, which conceptually expresses the ratio of signal and noise powers. For a single sensor,

$$SNR = \frac{\varepsilon\left[s^2(t)\right]}{\varepsilon\left[n^2(\vec{0},t)\right]} = \frac{R_s(0)}{R_n(\vec{0},0)} \tag{3.46}$$

where $R_s(0)$ and $R_n(\vec{0},0)$ are the spatial correlation matrices of the signal and noise components respectively. When an array of M sensors is employed, the signal measured by the mth sensor is $y_m(t) = s(t - \vec{\alpha}^0 \cdot \vec{x}_m) + n(\vec{x}_m,t)$. The delay-and-sum beamformer's output signal thus equals

$$z(t) = \sum_m w_m y_m(t - \Delta_m) = \sum_{m=0}^{M-1} w_m s(t - \Delta_m - \vec{\alpha}^0 \cdot \vec{x}) + \sum_{m=0}^{M-1} w_m n(\vec{x}_m, t - \Delta_m) \tag{3.47}$$

The *array signal-to-noise ratio* is the ratio of mean-sqaured values of the signal and noise terms. Regarding the signal and noise as uncorrelated random processes, these mean-squared values are

$$\textit{Signal}: \sum_{m_1=0}^{M-1}\sum_{m_2=0}^{M-1} w_{m_1} w_{m_2}^{*} R_s(\Delta_{m_2} - \Delta_{m_1} - \vec{\alpha}^0 \cdot (\vec{x}_{m_1} - \vec{x}_{m_2}))$$

$$\textit{Noise}: \sum_{m_1=0}^{M-1}\sum_{m_2=0}^{M-1} w_{m_1} w_{m_2}^{*} R_n(\vec{x}_{m_1} - \vec{x}_{m_2}, \Delta_{m_2} - \Delta_{m_1}) \tag{3.48}$$

where $R_s(\cdot)$ denotes the signal's correlation function and $R_n(\cdot,\cdot)$ the spatiotemporal correlation function of the noise. The array gain G is defined as the ratio of the array signal-to-noise ratio and the sensor signal-to-noise ratio.

$$G \equiv \frac{SNR_{array}}{SNR_{sensor}} \tag{3.49}$$

3.3.6 Minimum Redundancy Arrays

Minimum Redundancy Arrays (MRA) have been designed with tools from number theory and numerical search algorithms [25]. MRA design exploits the redundant structure of the uniform linear array for independent sources. MRA designs provide an effective aperture proportional to the square of the number of actual sensors, but the resulting arrays are constrained to be linear.

Consider a uniformly spaced linear array of M identical sensors which is illuminated by P incoherent sources with waveforms $\{s_1(t),\ldots\ldots\ldots, s_P(t)\}$, where

$$x_k(t) = \sum_{k=1}^{P} s_k(t)\exp\left(-j(k-1)\pi\sin\left(\theta_l\right)\right) + n_k(t) \tag{3.50}$$

where d is the sensor spacing, and the noise components $\{n_1(t),\ldots..n_M(t)\}$ are uncorrelated. The cross-covariance between sensor outputs can be expressed as

$$E\left\{x_m(t)x_n^*(t)\right\} = \sum_{k=1}^{P}\sigma_k^2\exp\left(-j(m-n)\pi\sin\left(\theta_l\right)\right) + \sigma^2\delta(m-n) \tag{3.51}$$

where σ^2 is the variance of the noise components, σ_k^2 is the power of the k th far-field source, and $\delta(m-n)$ is the Kronecker delta function. Equation (3.39) indicates that the

cross-covariance between two sensors can be interpreted as an integer which is difference of their locations, that is $E\{x_m(t)x_n^*(t)\} = r_{m-n}$. The steering vectors for the uniform linear array take the form

$$a(\theta) = \left[1, \exp(-j\pi\sin(\theta)), \ldots\ldots, \exp(-j(M-1)\pi\sin(\theta))\right]^T \tag{3.52}$$

because of this form of the steering vectors, the array covariance matrix R is Toeplitz. which implies that if we can compute the set of covariances $\{r_0, r_1, \ldots\ldots, r_{M-1}\}$, then we can reconstruct R due to the Toeplitz property. A arbitrary M x M covariance matrix has $M(M+1)/2$ parameters due to the fact that $R = R^H$. When the covariance matrix is constrained to be Toeplitz, the number of free parameters reduces to M. Therefore it is possible to remove some of the M sensors, and still be able to compute R from the remaining sensor measurements.

3.3.7 Solid Collection Angle

The solid collection angle of the array is defined as

$$\text{solid collection angle} = \tan^{-1}\left(\frac{Md}{2r^0}\right) \tag{3.53}$$

The solid collection angle of the array defines the angular separation in which the sound source should be placed for the array beamforming results to produce a mainlobe width which is half the value of the lobe width at one-half the peak value.

Chapter 4

EQUIPMENT AND EXPERIMENTAL PROCEDURE

4.1 Equipment

4.1.1 Measurement System

The twelve microphones used for acoustic measurements were Bruel & Kjaer® Type 4136 microphones. Each had a diameter of ¼-inch. The microphones possessed a sensitivity of 1.6 mV/Pa, and had a flat response in the frequency range of 4Hz to 70kHz. The microphones had a dynamic range of 47 to 172dB when connected with Bruel and Kjaer® Preamplifier Type 2670. Preamplifier Type 2670 had an operational frequency range of 3Hz to 200kHz and a typical attenuation of 0.25dB. The microphones and preamplifiers were powered by Bruel and Kjaer® Multiplexer Type 2822 which had differential outputs to avoid ground loops. It had twelve channels and a frequency response of 2Hz to 200kHz (±0.3dB). The outputs of the multiplexer were connected to a digital data acquisition hardware called the IOTECH® WAVEBOOK/512 system. This system comprised of a 8-channel, 12-bit resolution, 1MHz sampling rate A/D board. The WAVEBOOK/512 also included the WaveView software which is a WINDOWS-based software. This setup and acquisition system allowed one to configure, display, and save data to disk. The WBK20 PC-Card/EPP (enhanced parallel port) interface card & cable

was incorporated in the WAVEBOOK/512 for an enhanced rate of data transfer between the data acquisition system and the computer connected to it. For data analysis, a 300-MHz WINDOWS-NT machine was used. A schematic diagram of the measurement system is shown in Figure 4.1.

The sound source was a six and a half inch diameter Radio Shack® woofer mounted on one wall of a Plexiglas box with the opposite wall of the box containing a 2 inch diameter hole for the propagation of sound waves produced by the woofer. The wall on which the woofer was mounted was movable, and in this way the Plexiglas box functioned as a Helmholtz Resonator capable of magnifying sound pressure levels produced by the woofer in the frequency range of interest. Described below is the procedure adopted for designing the Helmholtz resonator and the physical dimensions of the designed resonator.

4.1.2 Design of the Acoustic Driver

The elements of a Helmholtz resonator are a closed volume V with rigid walls , and a small opening of area A and length l connecting it to a much larger volume [26]. A schematic diagram of a typical Helmholtz resonator is shown in Figure 4.2. The resonant frequency of a Helmholtz resonator depends on the enclosed volume and the size of the opening. When pressure fluctuations, $p_{i,o}$, outside the resonator excite the volume of the air inside the neck of the opening at the resonant frequency, the sound pressure, p_b,

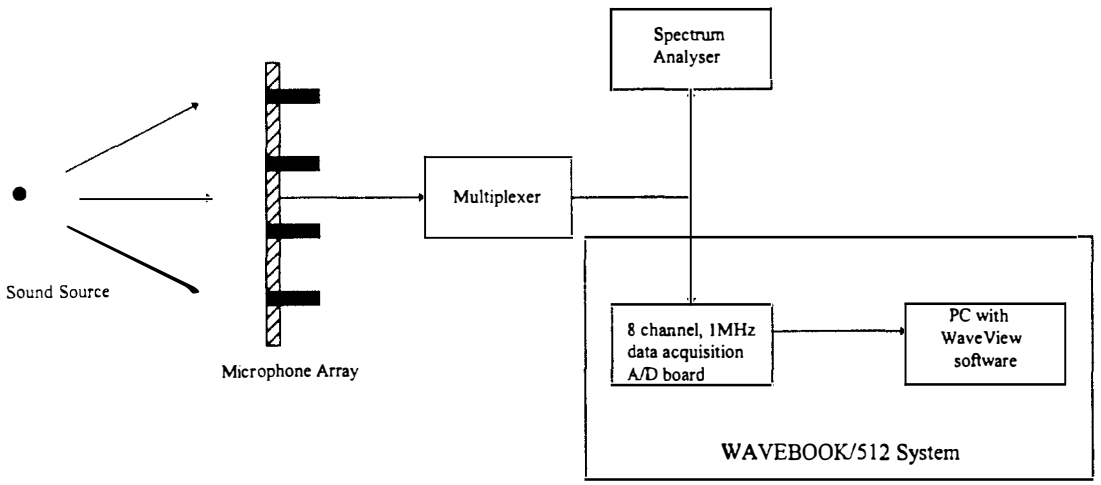

Figure 4.1 Schematic Diagram of the Measurement System

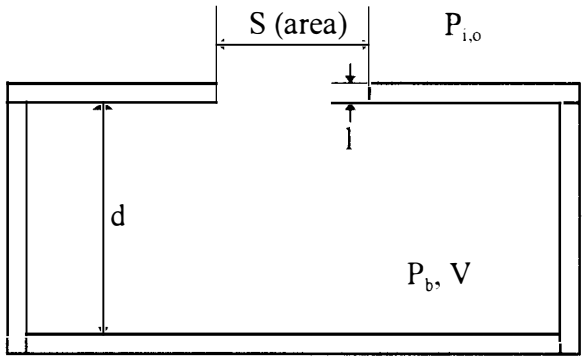

Figure 4.2 Schematic representation of a Helmholtz resonator

inside the cavity increases to a level that is much greater than the sound pressure level outside the cavity.

The volume of air located in the neck of the opening moves in and out of the cavity. This varies the volume of the resonator cavity which in turn varies the pressure inside the cavity. This pressure variation is termed p_h. The displacement, d, of the air in the neck is related to the acoustic pressure outside the cavity by the following equation

$$d = \frac{p_{i,o}}{\rho\left(\frac{c^2 A}{V} - 4\pi^2 f^2 l\right)} \sin(2\pi f t) \tag{4.1}$$

where ρ is the density of air, c is the speed of sound in air, A is the area of the opening, V is the volume of the cavity, f stands for the frequency of the incident pressure fluctuations, l denotes the length of the neck of the opening and t is the time.

The acoustic pressure inside the cavity is related to the displacement of air in the neck by the following equation

$$p_h = d\rho c^2 AV \tag{4.2}$$

Solving equations (4.1) and (4.2) for p_h, we obtain

$$p_h = \frac{c^2 A}{V\left(\frac{c^2 A}{V} - 4\pi^2 f^2 l\right)} p_{i,o} \sin(2\pi f t) \tag{4.3}$$

From equation (4.3) it is evident that when $\frac{c^2 A}{V} = 4\pi^2 f^2 l$, the acoustic pressure inside the cavity goes to infinity. However, in practice, frictional and viscous resistance

inside the neck limit the acoustic pressure to a large but finite value. The frequency at which equation (4.3) becomes infinite is called the resonant frequency and is given by

$$2\pi f_R = \left(\frac{c^2 A}{lV}\right)^{\frac{1}{2}} \tag{4.4}$$

where f_R is the resonant frequency of the Helmholtz resonator.

For this work, a Helmholtz resonator (driver) (Figure 4.3) was constructed out of Plexiglas to magnify the amplitudes produced by the woofer in the frequency range of 800-1100Hz. The length and width dimensions of the enclosed volume were 7.5 inches each. The circular opening had a diameter of 2 inches and the neck of the opening was 1/8-inches. The depth dimension *d* of the enclosed volume was designed to be variable by mounting the woofer on a Plexiglas plate which could move inside the resonator. The design values of *d* for frequencies in the 800-1100Hz range are tabulated in Table 4.1. The woofer was rated at 92 ± 2 dB/W/m in the frequency range of 50-6000Hz, and had a power handling capacity ranging between 20 and 40 Watts. The woofer was driven with an amplifier, a function generator being used as the waveform source.

4.1.3 Microphone Array Details

Two linear microphone arrays were designed to measure the Sound Pressure Levels produced by the model. The two microphone arrays were - (1) the seven microphone uniformly spaced linear array, and (2) the minimum redundancy linear array.

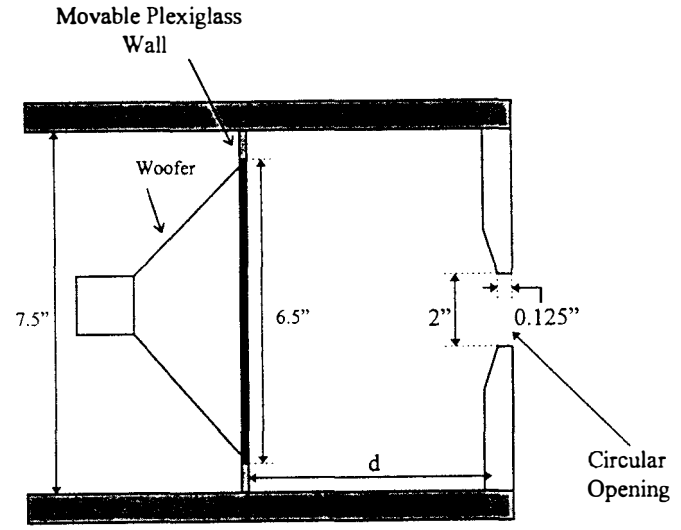

Side View

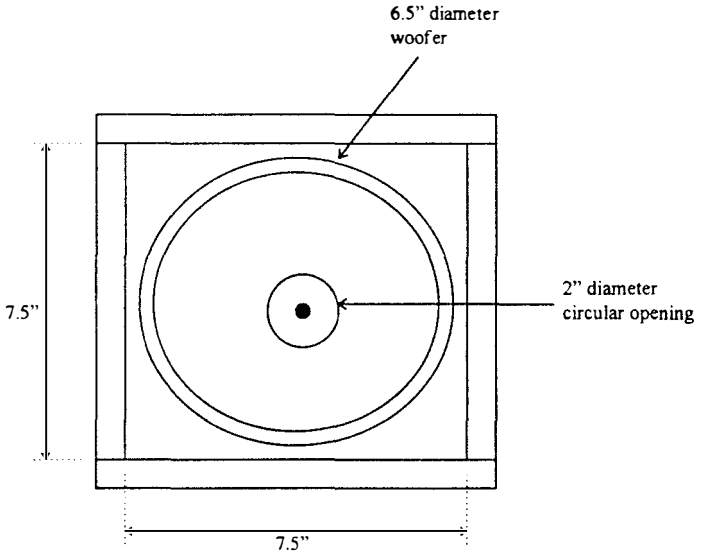

Front View

Figure 4.3 Dimensions of the Designed Driver

Table 4.1 Design values of “d” for the Driver

frequency (Hz)	d (in)
800	4.2
900	3.2
1000	2.5
1100	2.1

The uniformly spaced linear array consisted of seven flush mounted microphones separated by a spacing of ½-inch as shown in Figure 4.4. To avoid spatial aliasing, the sensor separation must be lesser than or equal to $\lambda^0 / 2$ where λ^0 denotes the wavelength of the propagating signal. The upper-frequency limit of the frequency range of interest, i.e., 1100Hz was used to determine the sensor spacing. The linear array had a gain of approximately 8.5 dB.

Minimum Redundancy Arrays (MRA) can be used to increase the effective aperture of uniform linear arrays [30]. These arrays are designed with tools from number theory and numerical search algorithms. MRA design exploits the redundant structure of the uniform linear array for independent sources. MRA designs provide an effective aperture proportional to the square of the number of actual sensors and the resulting array is constrained to be linear. For this work, a four microphone non-redundant linear array was constructed by eliminating redundant sensors in the seven microphone uniform linear array. This array had a gain of approximately 6 dB. The four microphone Minimum Redundancy Array is shown in Figure 4.5.

A one arm two dimensional spiral array with ten microphones was also designed for acoustic measurement, the details of which are given in Appendix A.

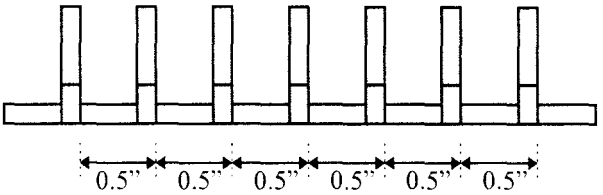

Figure 4.4 Uniformly Spaced Seven-Microphone Linear Array

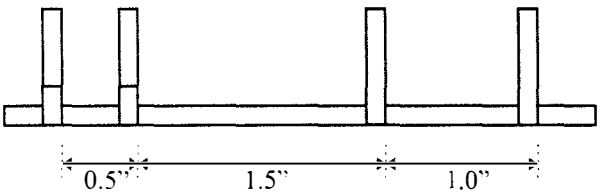

Figure 4.5 Four-Microphone Minimum Redundancy Linear Array

4.2 Experimental Procedure

4.2.1 Calibration

All the microphones used in the arrays and as singular microphones were calibrated using the "Quest LC" sound source which produces a constant Sound Pressure Level (SPL) of 114 dB at a 1000Hz. The calibration results showed that the microphones measured the SPL of the sound source within 3 dB of the rated SPL at a 1000 Hz. A typical plot of the SPL versus frequency obtained from a microphone calibration is shown in Figure 4.6.

The driver was calibrated by measuring the SPL produced by it in the frequency range of 800-1100Hz. A ¼-inch Bruel and Kjaer® microphone was positioned at a distance of 1-inch from the neck of the circular opening of the driver. SPL measurements were then made by setting the design values of d at the corresponding frequencies as specified in Table 4.1. Figure 4.7 shows the spectrum of the microphone with the driver being driven at 1000Hz. A peak with a value of 122 dB is observed at 1000Hz. However, an equally strong second peak is observed at 3000Hz which is the second harmonic of the sound produced by the driver, implying that the driver is not a monochromatic source.

Smoke visualization tests were conducted near the opening of the driver to ensure that synthetic jet effects [30] were absent. Synthetic jets have the unique property of being zero-mass-flux in nature, that is, they are synthesized from the working fluid in the flow system in which they are embedded. The interaction of synthetic jets and an embedding flow near the flow boundary leads to the formation of closed recirculating

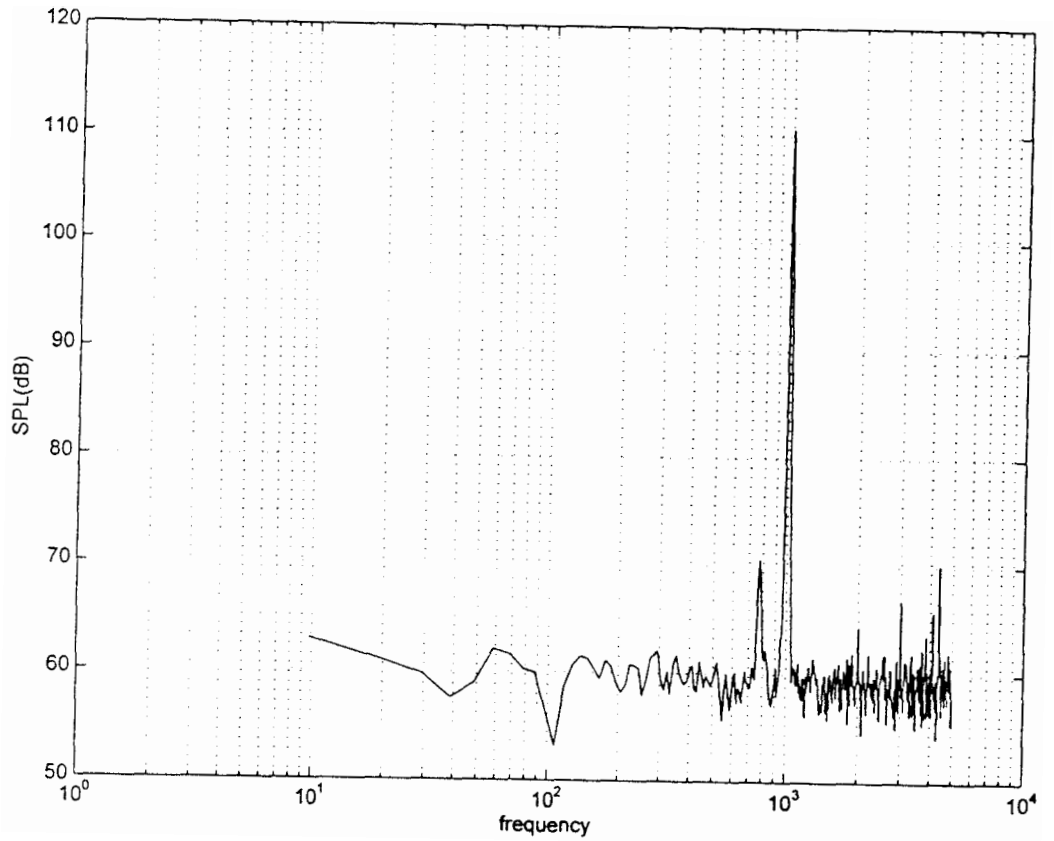

Figure 4.6 Spectrum of the Microphone Calibration

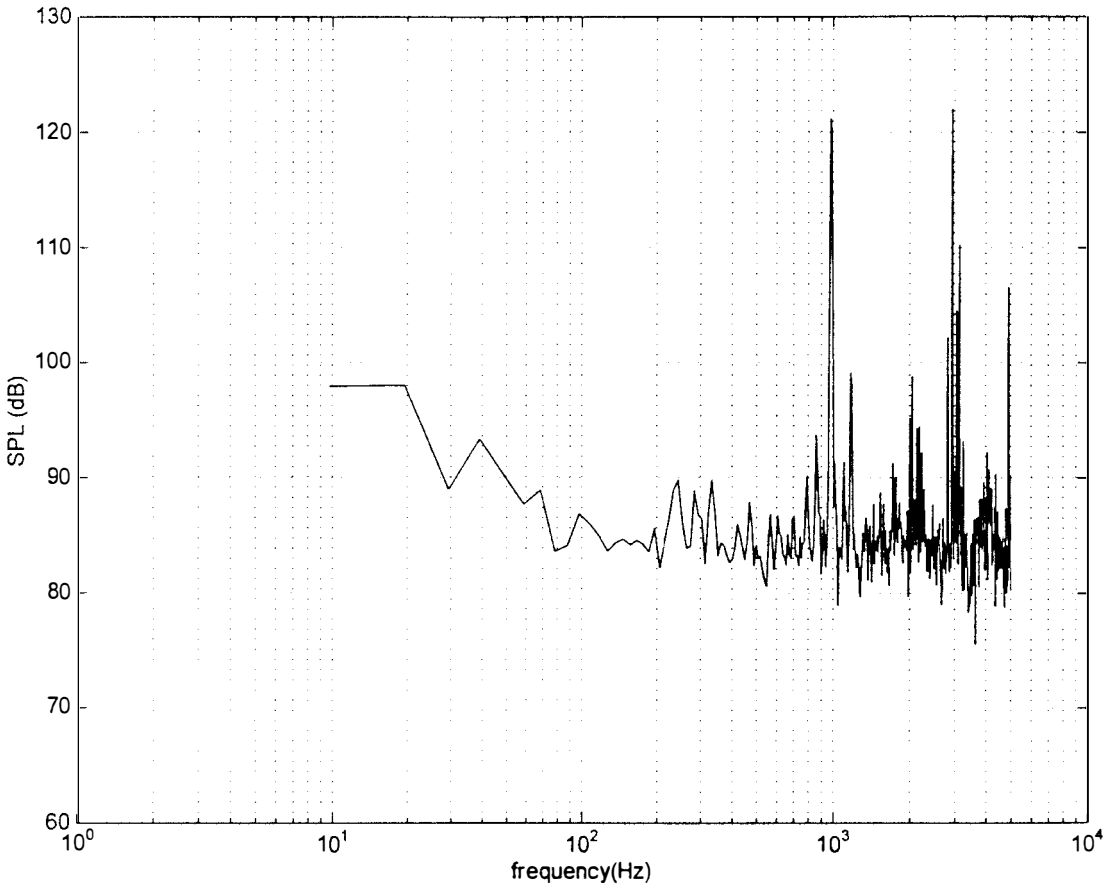

Figure 4.7 Spectrum of the Driver Calibration at 1000 Hz

regions. The smoke visualization tests were conducted to make sure that these recirculating regions were absent.

4.2.2 Open-Field Measurements

The two linear arrays and the spiral array were tested in the open field with the driver as the sound source placed in the same configuration relative to the arrays as it would be placed in the wind tunnel tests. Open field SPL measurements were made to provide a semianechoic result with which to compare the results obtained in the wind tunnel. A typical open field measurement setup is shown in Figure 4.8. Egg shell foam insulation was used as non reflecting boundaries on three sides of the open field test setup to minimize the interference of extraneous sound, and to reduce the effect of reverberation from hard surfaces. The strut-mounted rectangular block containing the flush mounted microphone array was positioned at a height of 14 inches above the ground to minimize the effect of reverberation from the ground. The center of the circular opening of the driver was placed at a distance of 20 inches from the flush mounted array. The sound source was elevated 14 inches above the ground such that a line joining the center of the circular opening of the sound source and the center of the array was parallel to the ground. The five positions of the sound source relative to the microphone array for which the open field SPL measurements were conducted are shown in Figure 4.8.

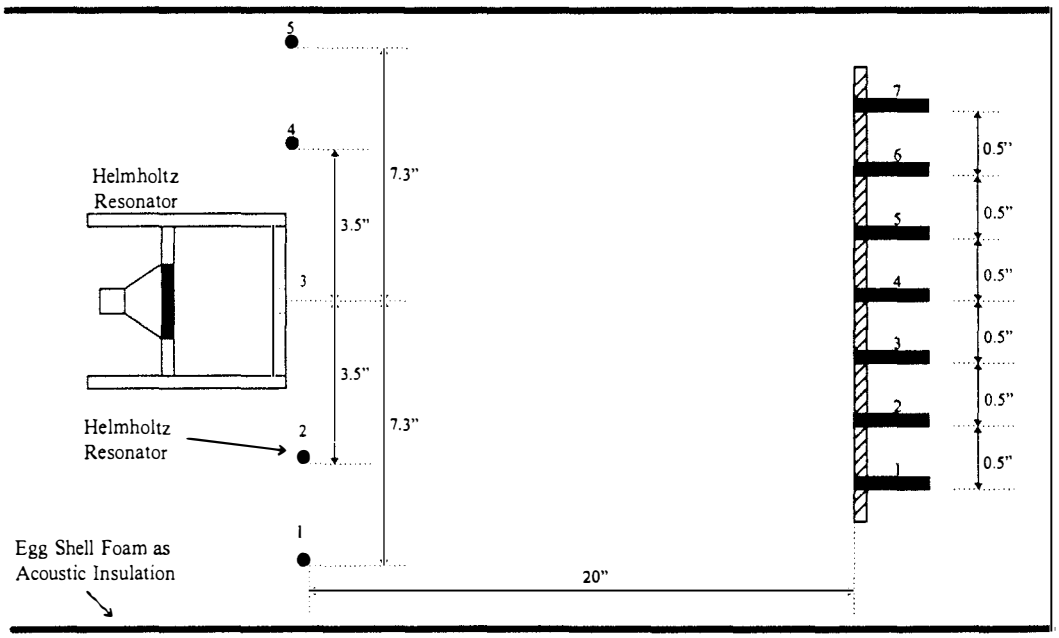

Figure 4.8 Schematic Diagram of the Open Field Test Setup

4.2.3 Wind Tunnel Measurements

The arrays were mounted on the sidewall of the 20"x14"x40" test section of the UTSI (University of Tennessee Space Institute) low speed wind tunnel, and the wind tunnel background noise was measured for different tunnel velocities in the absence of the driver. After the characterization of the background noise of the wind tunnel was complete, the driver was mounted on the sidewall of the test section opposite to that on which the arrays are mounted as shown in Figure 4.9. The position of the driver relative to the microphone arrays was the same as in open field tests. SPL and direction of arrival measurements were made for different combinations of sound wave frequencies, driver locations, and tunnel speeds. The SPL and direction of arrival results were compared with the corresponding open field results .

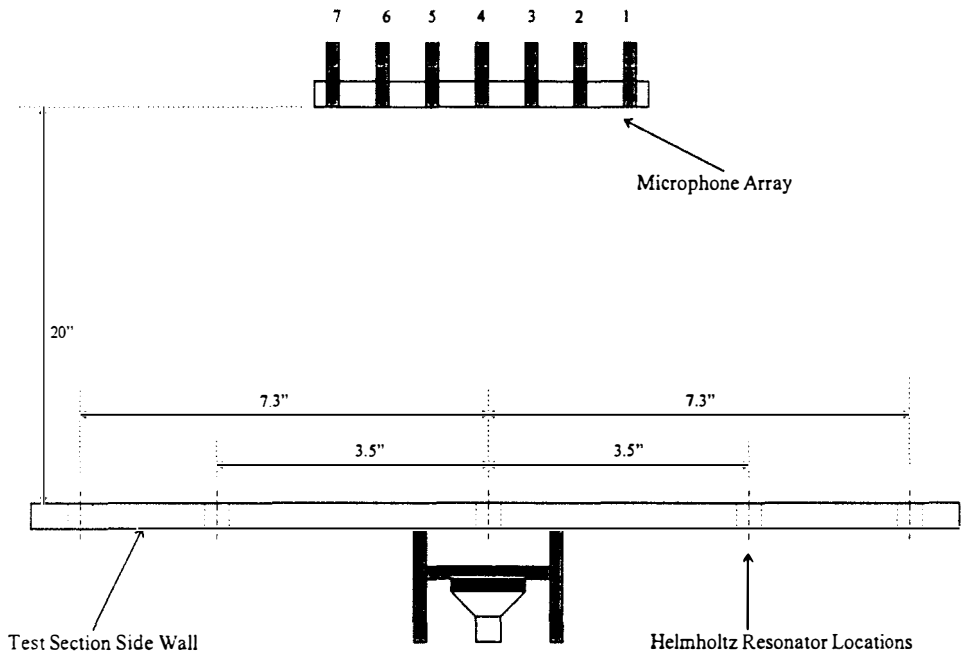

Figure 4.9 Wind Tunnel Test Setup with Driver

4.3 Data Post-Processing Procedure

4.3.1 Cross-Spectral Matrices

An M by M cross spectral matrix, where M is the total number of microphones in the array, was first constructed for each data set. The formation of the individual matrix elements was achieved through the use of Fast Fourier Transforms (FFT). Each channel of data was then segmented into a series of non-overlapping blocks each containing 1024 samples. Using a Hanning window, each of these blocks was Fourier transformed into the frequency domain. The individual upper triangular matrix elements plus the diagonal were formed by computing the corresponding block-averaged cross spectra from the frequency data using

$$G_{ij}(f) = \frac{1}{N}\sum_{k=1}^{N}\left[X_{ik}^{*}(f)X_{jk}(f)\right] \tag{4.6}$$

where N is the number of blocks of data, and X represents an FFT data block. The lower triangular elements of the cross-spectral matrix were formed by taking the complex conjugates of the upper triangular elements, because the cross-spectral matrix is Hermitian.

4.3.2 Beamforming

A classical beamforming approach is used for the analysis. The basic procedure consists of electronically steering the array to a predefined series of steering locations in space. For each selected steering location, a steering matrix $\hat{e}$ containing one entry for

each microphone in the array was computed. Using the steering matrix for the steering location and the cross-spectral matrix computed previously, the steered array output power at the steering location was given by

$$P(\hat{e}) = \frac{\hat{e}^{T}\left(\hat{G}_{data} - \hat{G}_{background}\right)\hat{e}}{M} \tag{4.7}$$

where the T denotes the conjugate transpose of the matrix. The background spectra $G_{background}$, was that obtained without the tunnel flow, where the acquisition system electronic noise dominates the recorded output.

Chapter 5

Results and Discussion

5.1 Open Field Test Results

Open field tests were conducted with the three array configurations to provide a semianechoic reference with which to compare the reverberation affected performance of the arrays inside the wind tunnel.

The center of the Helmholtz resonator sound source (driver) was placed at positions numbered 1 through 5 as shown in Figure 4.9 (pp. 55). The driver positions 1, 2, 3, 4, and 5 were at an angle of 105°, 95°, 85°, 75°, and 65° respectively from the line joining the array microphones with microphone 1 as the origin. The angles were measured in the counter-clockwise direction.

Figure 5.1 is a semilogarithmic plot of the measured Sound Pressure Level at the array versus the frequency for an open field measurement, conducted with the driver placed at position 1, and driven at 1000 Hz. The plot shows a peak equal to 112 dB at 1000 Hz corresponding to the sound produced by the source. Also observed in the plot is a peak equal to 115dB at 3000 Hz. This peak at 3000 Hz is the second harmonic of the sound produced by the source.

Figure 5.2 (a) and 5.2 (b) show a plot of the measured SPL versus the look direction, called a Direction Of Arrival (DOA) plot, for position 1 of the sound source

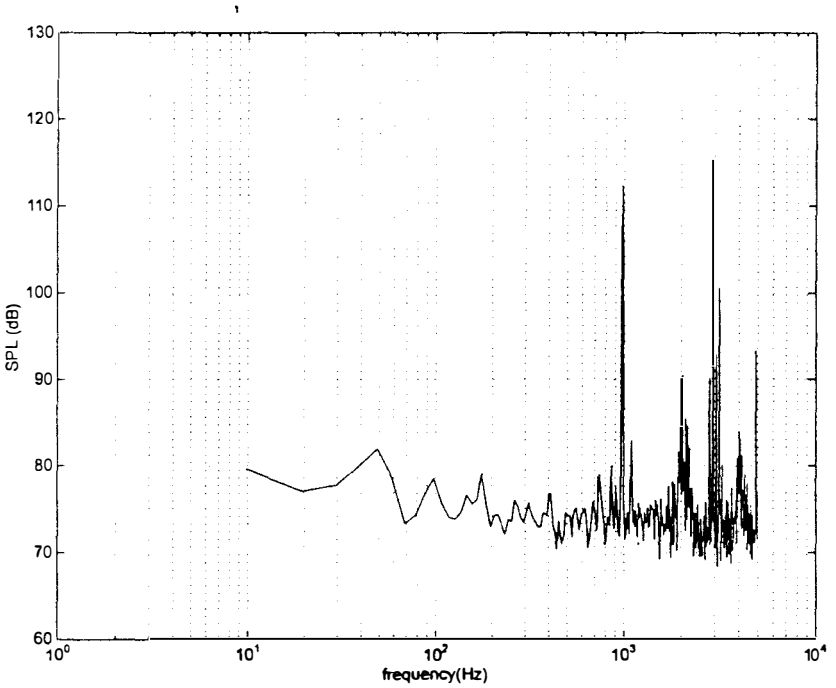

Figure 5.1 Spectrum of the Uniform Linear Array, Driver at Position 1 (105°), Open Field Test

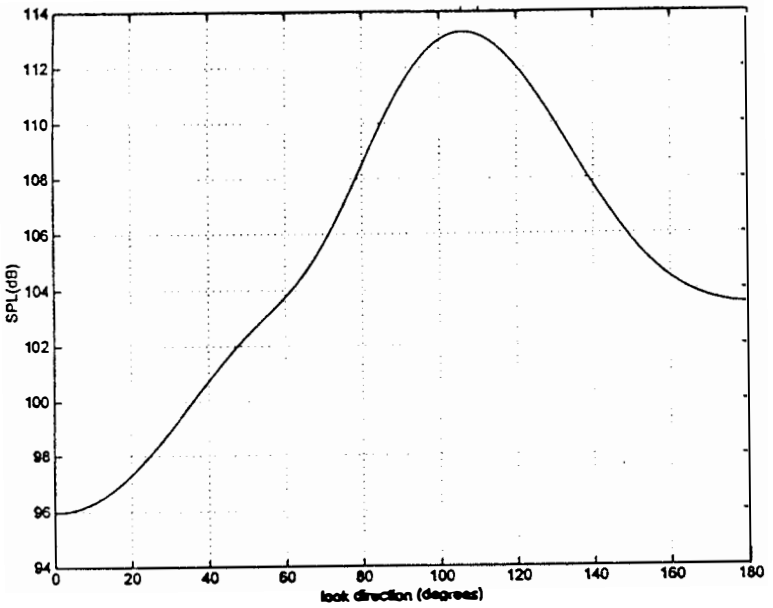

(a)

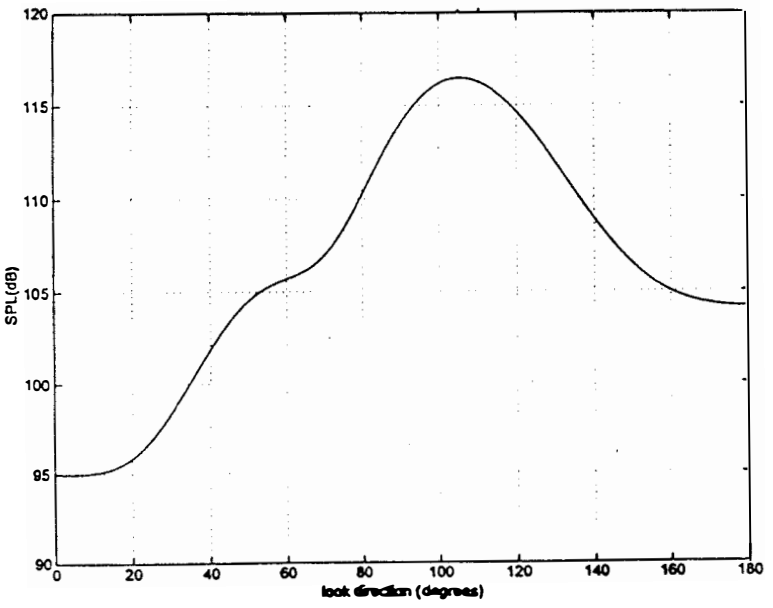

(b)

Figure 5.2 DOA plot for the (a) Uniform Linear Array, (b) MRA, Driver at Position 1 (105°), Open Field Test

corresponding to an angle of 105° for the 7-microphone uniform linear array(uniform linear array) and the four microphone minimum redundancy array respectively. The SPL measured at 105° by the two arrays is within 4 dB of the SPL of the power spectrum shown in Figure 5.1. Another observation made from a comparison of the DOA plots shown in Figures 5.2 (a) and 5.2 (b) is that the MRA measures an SPL of 117 dB at 105° which is 4 dB higher than that measured by the uniform linear array. This is due to the increased effective aperture of the MRA over the uniform linear array discussed earlier. The resolution of the SPL peak at 105° for the MRA from the nearest local maximum at 180° is about 12 dB which is 3 dB higher than that measured by the uniform linear array.

Figures B.1, B.2, B.3; figures B.4, B.5, B.6 ; figures B.7, B.8, B.9 and figures B.10, B.11, B.12 found in Appendix B display the power spectra and the DOA plots obtained from the two linear arrays for sound source positions 2 through 5 respectively. A plot of the look direction prediction error versus the actual look direction of the driver shown in Figure 5.3 shows that the two array configurations measure the look direction of the sound source accurate to within 3° of the actual position of the center of the driver.

The error in the look direction is attributed to the fact that the sound source is not an ideal point source. Another source of error could be the improper positioning of the sound source relative to the array. The maximum SPL measured by the uniform linear array for sound source positions 1 through 5 increased from position 1 through 3 due to the increased proximity of the sound source from the array and decreased from position 3 through 5 (Figure 5.4) as the distance of the sound source from the arrays increased.

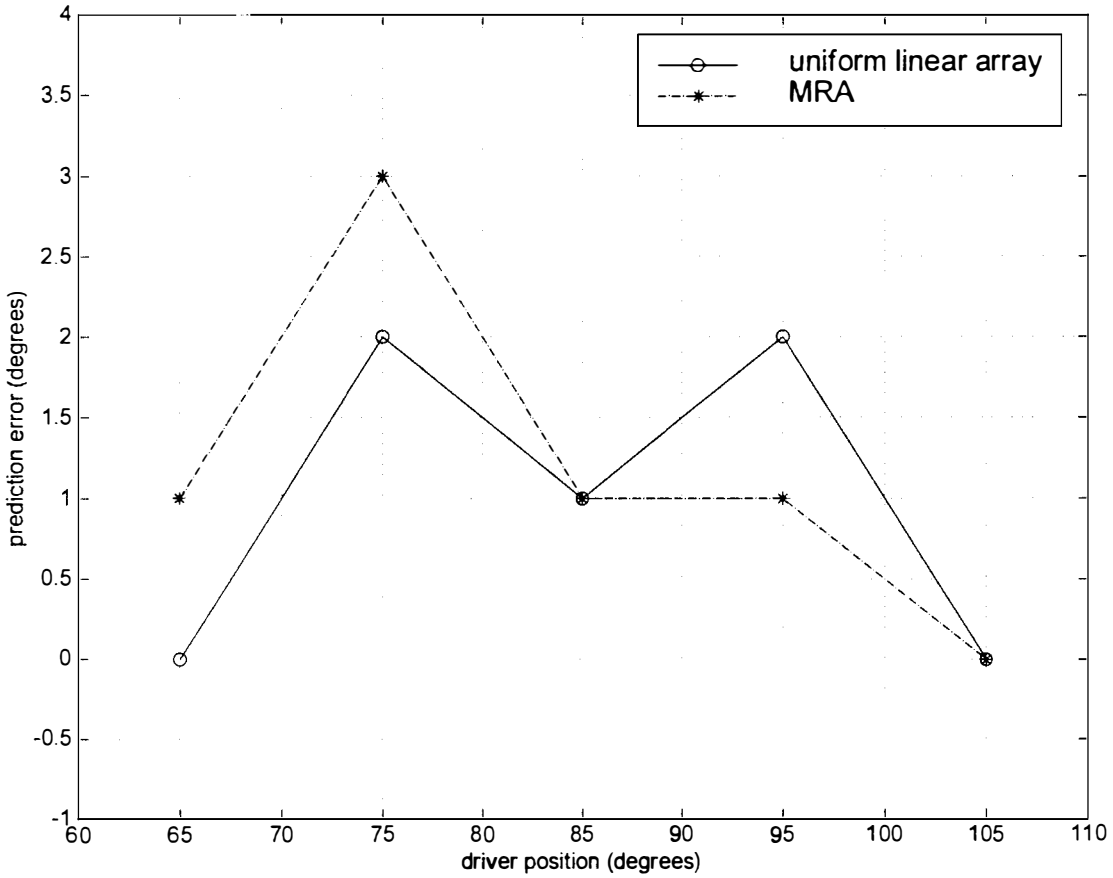

Figure 5.3 Plot of the Look Direction Prediction Error versus Actual Look Direction for the Driver Placed in the Open Field

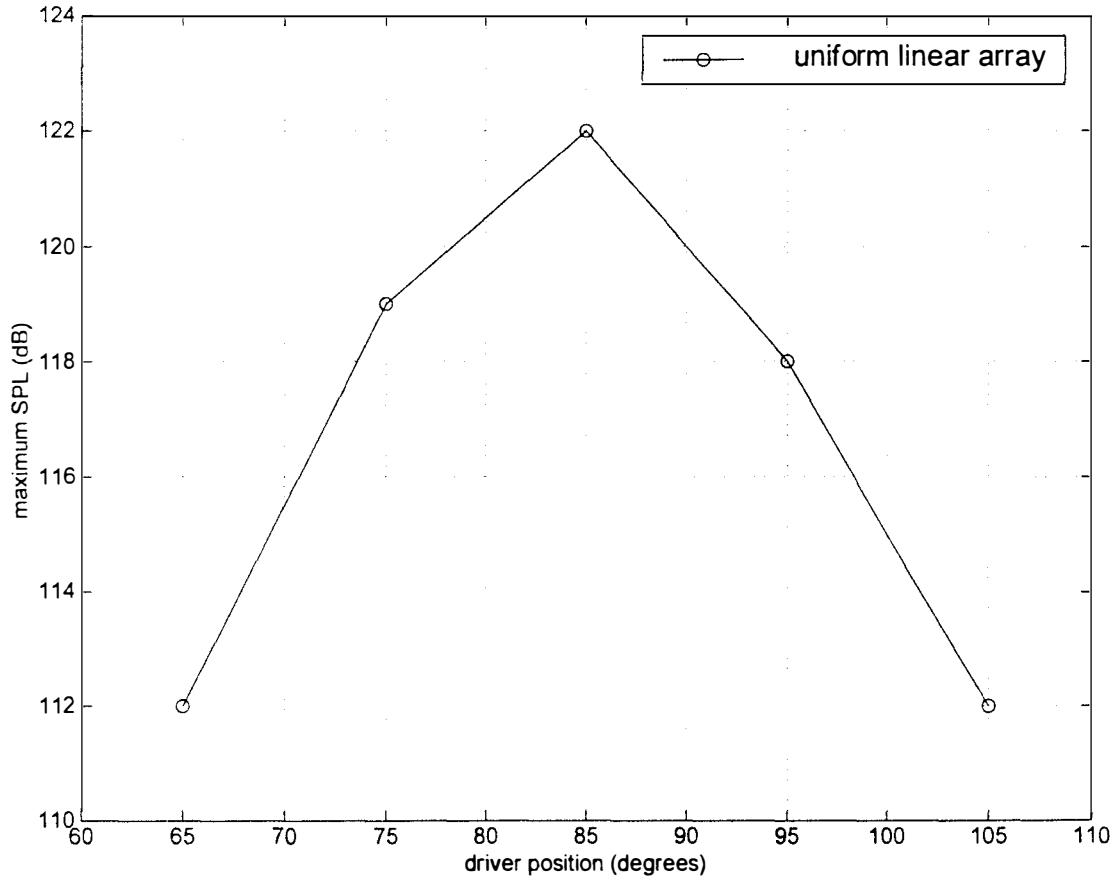

Figure 5.4 Plot of the Maximum SPL versus Actual Look Direction of the Driver in the Open field

The highest value of the SPL measured by the uniform linear array is 117 dB when the sound source was at position 3 corresponding to an angle of 85° which is 7 dB higher than that measured with the sound source at position 5 corresponding to a 65° angle. The MRA measured the highest SPL of about 122 dB with the source at 85° which is about 9 dB higher than that measured with the source at 65°.

5.2 Empty Wind Tunnel Test Results

The empty tunnel was run at tunnel velocities ranging from 45ft/sec to 151 ft/sec and the SPL measured using the uniform linear array. These tests were conducted so that any peaks produced by the tunnel fan or the tunnel background noise could be identified and distinguished from the peaks produced either by the driver or the cavity.

Figure 5.5 shows the power spectrum of the empty tunnel with the tunnel velocity at 45 ft/sec. The plot displays a peak at 1500 Hz corresponding to the carrier frequency of the frequency controller used to vary the wind speeds inside the wind tunnel. An ICP® Accelerometer Model 353B01 was adhesive mounted on the tunnel wall to verify that the peak at 1500 Hz is indeed due to the carrier frequency of the frequency controller and not due to flow disturbances in the tunnel. After a positive verification, it was decided to filter out the peak at 1500 Hz. Figure 5.6 shows the spectrum of the empty tunnel running at 45 ft/sec with the peak at 1500 Hz notch filtered. Figures 5.7 and 5.8 show the notch filtered spectra of the empty tunnel running at 81 and 151 ft/sec respectively.

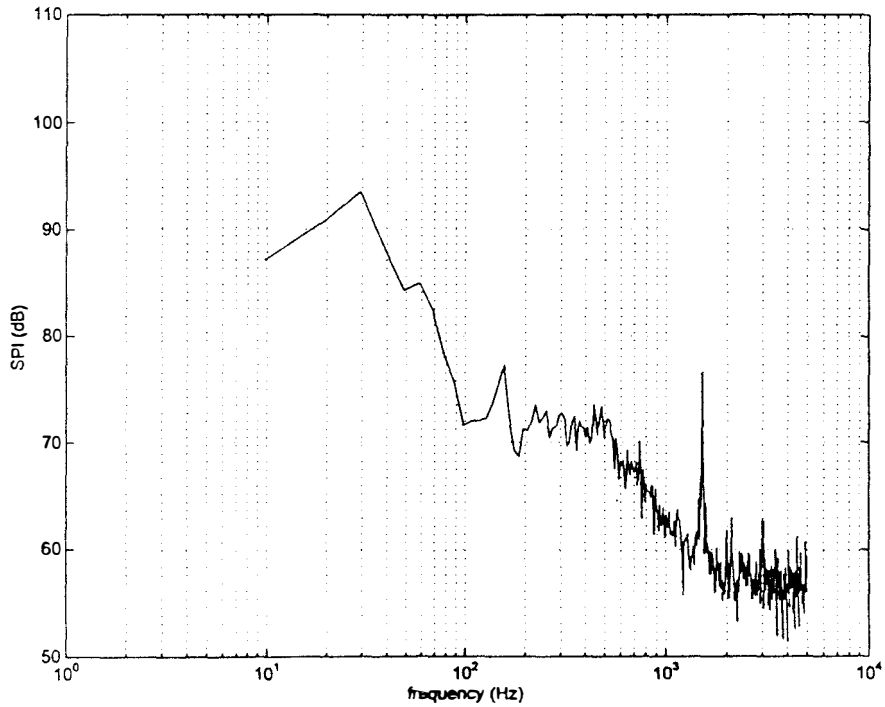

Figure 5.5 Empty Tunnel Array Spectrum, v = 45 ft/sec. Notch Filtering not Applied at 1500 Hz

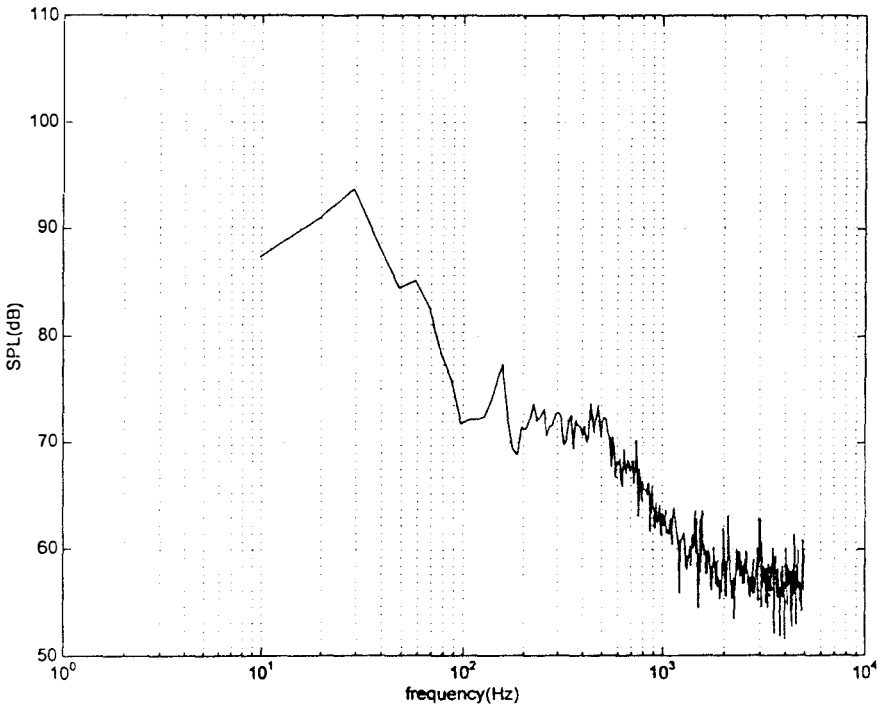

Figure 5.6 Empty Tunnel Array Spectrum, v = 45 ft/sec, Notch Filtering Applied at 1500 Hz

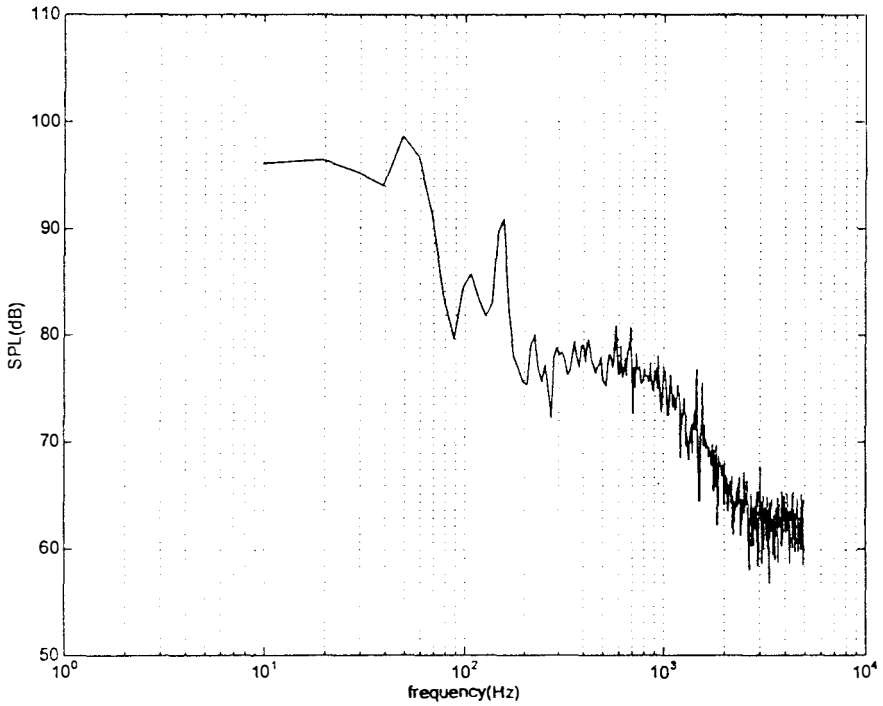

Figure 5.7 Empty Tunnel Array Spectrum, v = 81 ft/sec. Notch Filtering Applied at 1500 Hz

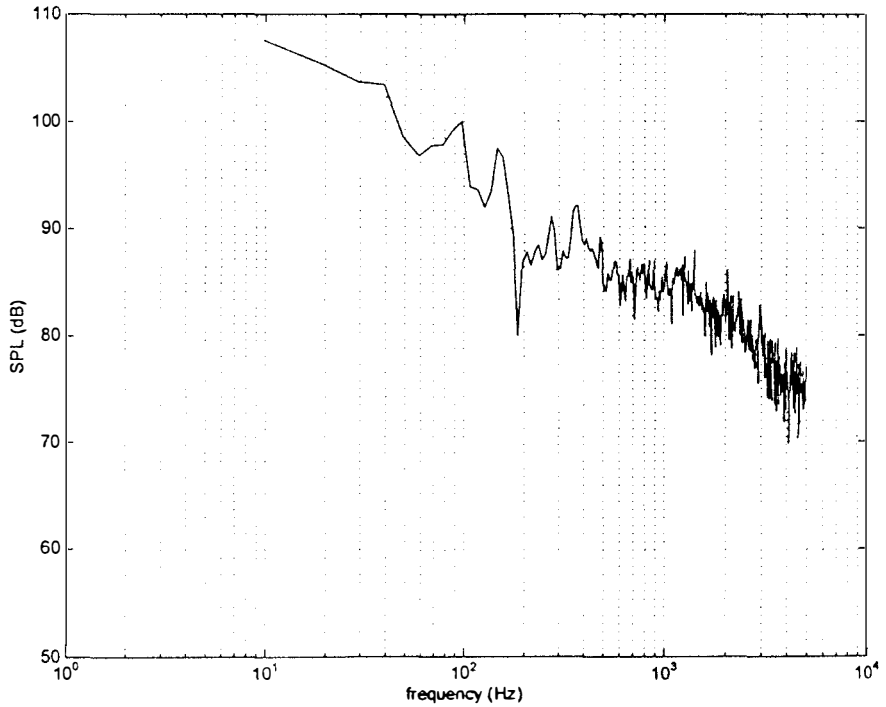

Figure 5.8 Empty Tunnel Array Spectrum, v = 151 ft/sec. Notch Filtering Applied at 1500 Hz

5.3 Measurements with Driver in Wind Tunnel

To evaluate the performance of the two linear arrays in a reverberant environment like a wind tunnel test section, and to verify the effect of wind velocity on the beamforming algorithm, the driver was mounted on the sidewall of the test section with the arrays mounted on the opposite wall as shown in Figure 4.10 (pp. 57). The positions of the driver relative to the arrays in the wind tunnel were identical to the positions in the open field test. This facilitated a comparison of the wind tunnel results with the semianechoic results provided by the open field test configurations.

Figure 5.9 is the power spectrum of the uniform linear array, with the driver at position 5 (65°) being driven at 1000 Hz and no flow in the wind tunnel. The spectrum shows a peak of 125 dB at 1000 Hz corresponding to the sound produced by the driver, and its second harmonic is reflected in the plot as a peak equal to 133 dB at 3000 Hz. The 125 dB peak at 1000 Hz represents an increase of approximately 13 dB over the open field measurement for position 5 (65°). The increase in SPL is attributed to the effect of reverberant energy in the wind tunnel test section. Figure 5.10 is the DOA plot for the uniform linear array with the driver at position 5 (65°) for the no flow condition. The plot shows a DOA peak equal to 127 dB at 70° which is 5° off the actual position of the driver. The error may be due to the improper positioning of the driver, and the presence of a multipath environment inside the wind tunnel. The SPL peak resolution from the nearest local maximum at 180° is 9 dB which is 2dB lower than that measured in the

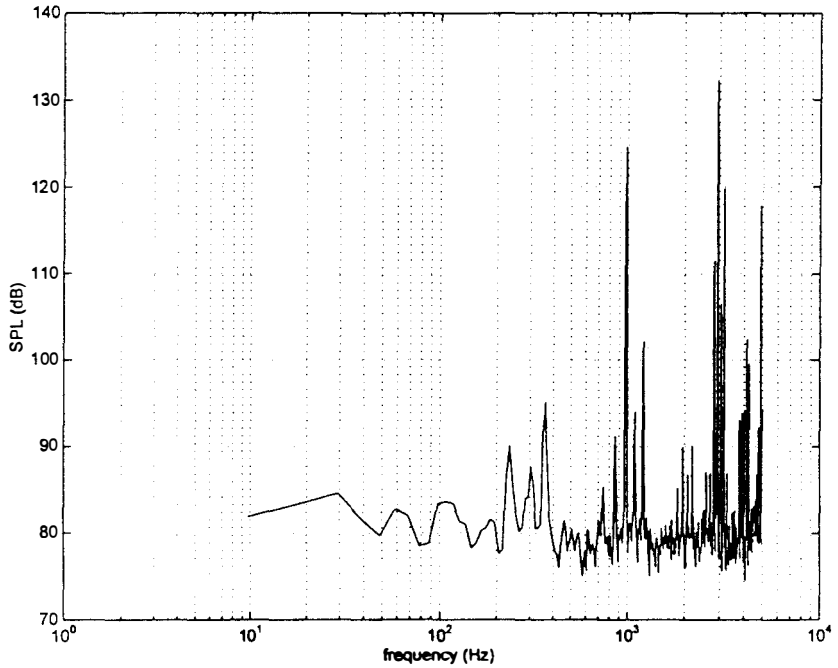

Figure 5.9 Spectrum of the Uniform Linear Array, Driver in Wind Tunnel at Position 5(65°), v = 0.

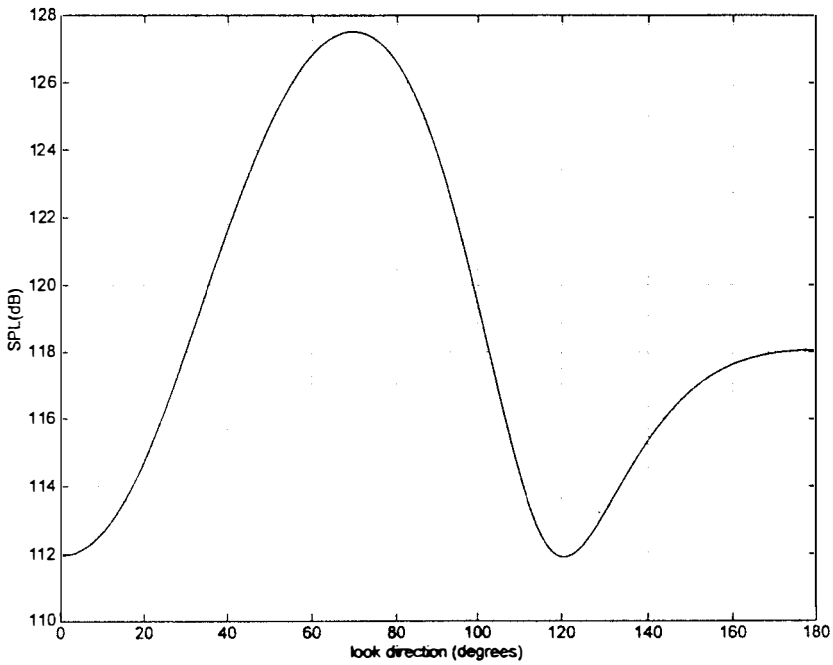

Figure 5.10 DOA Plot, Uniform Linear Array, Driver in Wind Tunnel at Position 5 (65°), $\nu = 0$.

open field. Figure 5.11 is a DOA plot for the MRA which measures a peak of approximately 132 dB at 70° and a resolution of 12 dB.

Figure 5.12 shows a semilogarithmic plot of the spectrum of the array with the driver at position 5 being driven at 1000 Hz and a tunnel velocity of 45 ft/sec. It is evident from the plot that there is an increase in the SPL in the frequency range of 100 to 900 Hz due to the effect of wind noise as compared to Figure 5.9 which is the spectrum at the no flow condition. Figure 5.12 shows a peak equal to 122 dB at 1000 Hz which is 3 dB lower than that shown in the no flow spectrum. This is attributed to the masking of the driver sound source by the wind noise. The peak produced at the tunnel carrier frequency of 1500 Hz has been notch filtered.

The DOA plot for the uniform linear array with no corrections made for the wind noise is shown in Figure 5.13 (a). The plot shows a DOA peak of 126 dB at a look direction of about 75° which is 10° off the actual driver position of 65°. The error is due to reverberation in the tunnel and the lack of a velocity correction procedure in the beamforming algorithm. The resolution is about 5 dB which is 4 dB less than the no flow case. Figure 5.13 (b) displays the DOA plot for the same configuration as above, but with the spectrum of the wind noise subtracted from the array spectrum. This plot shows a DOA peak of 122 dB at the same look direction as in Figure 5.13 (a), but with an improved resolution of 9 dB.

Figures 5.14 (a) and 5.14 (b) are the results for the MRA corresponding to the driver position and flow conditions represented in Figures 5.13 (a) and 5.13(b) respectively. The MRA measures a higher DOA peak than the uniform linear

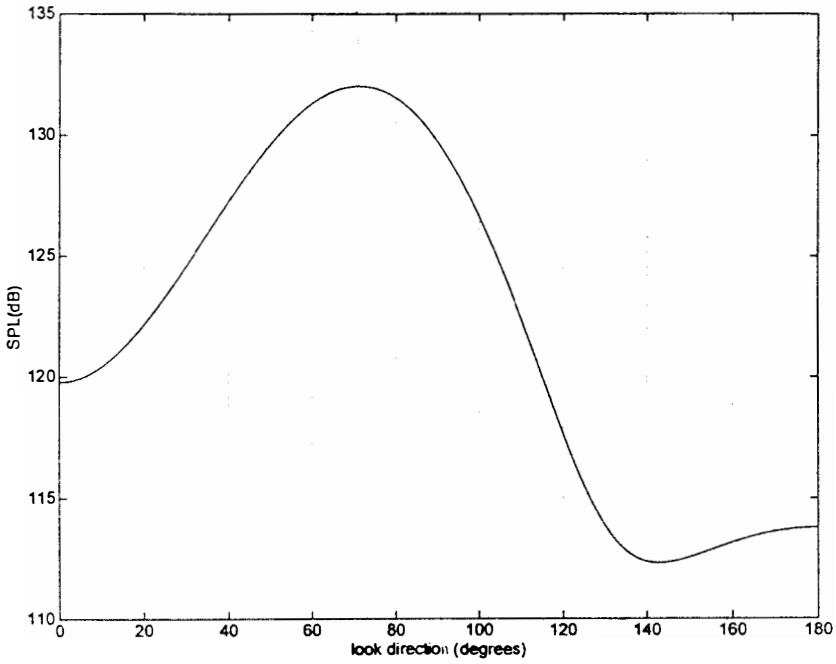

Figure 5.11 DOA Plot, MRA, Driver in Wind Tunnel at Position 5 (65°), v = 0

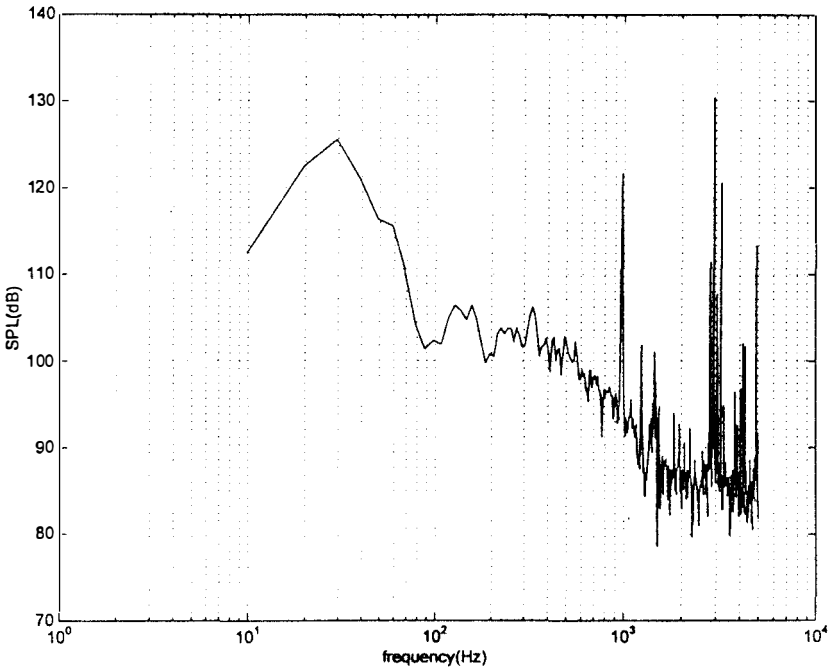

Figure 5.12 Spectrum of the Uniform Linear Array, Driver in Wind Tunnel at Position 5(65°), v = 45 ft/sec.

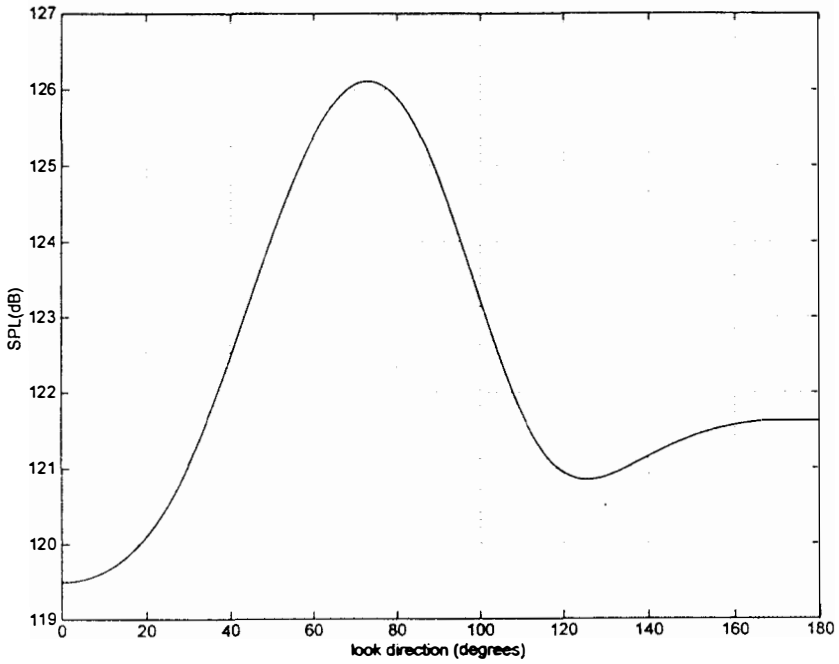

(a)

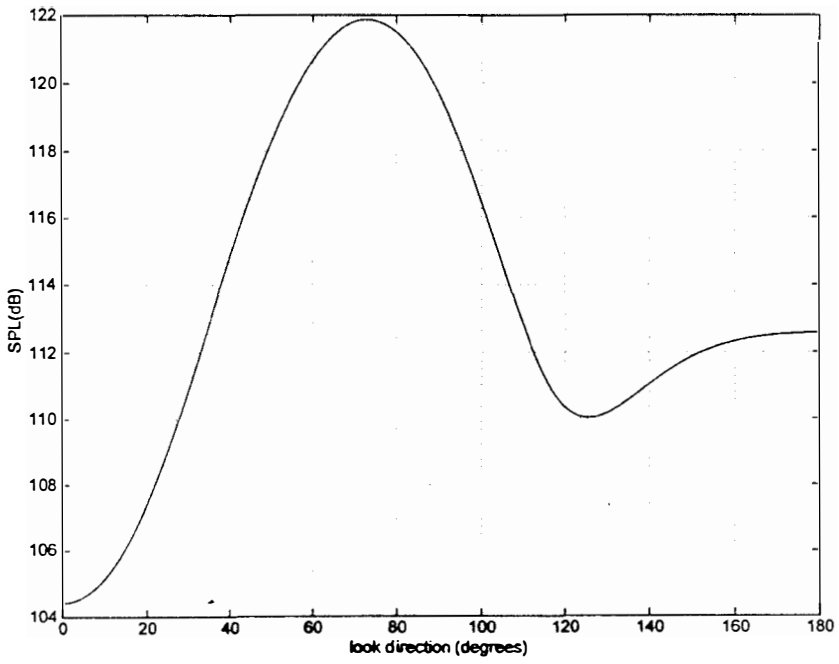

(b)

Figure 5.13 DOA Plot, Uniform Linear Array, Driver in Wind Tunnel at Position 5(65°), v = 45 ft/sec. (a) Wind Noise not Subtracted (b) Wind Noise Subtracted.

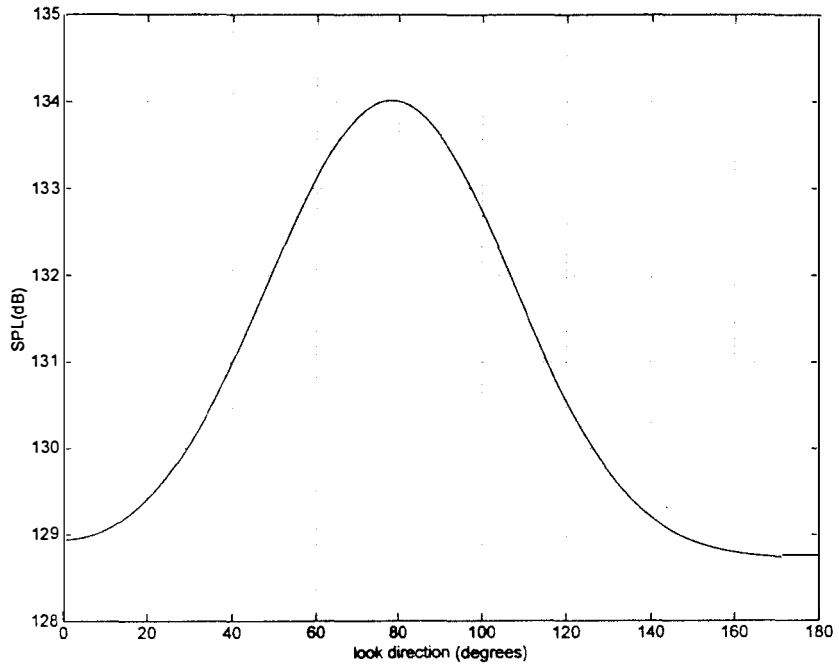

(a)

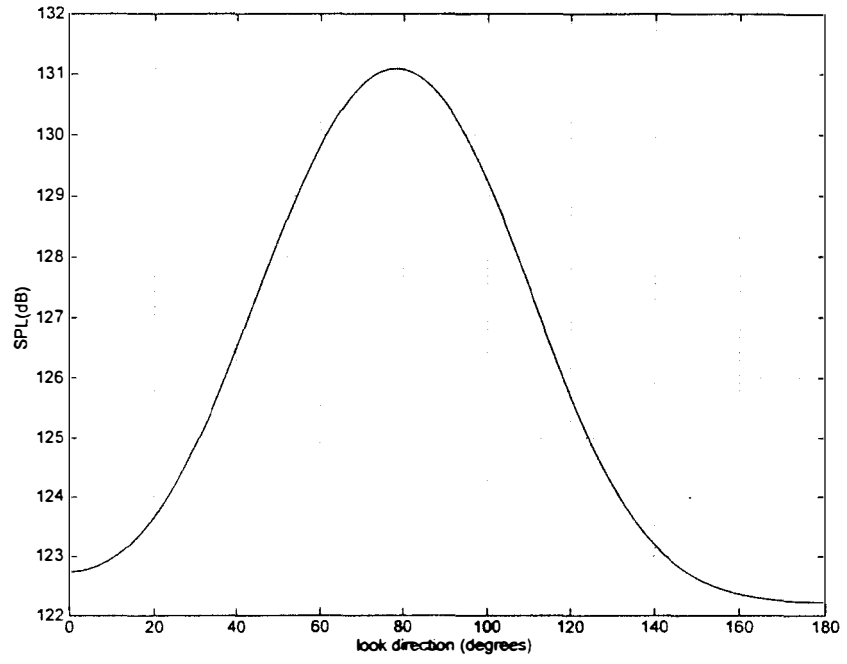

(b)

Figure 5.14 DOA Plot, MRA, Driver in Wind Tunnel at Position 5(65°), v = 45 ft/sec. (a) Wind Noise not Subtracted, (b) Wind Noise Subtracted.

array due to its increased effective aperture, and represents the same trends in the SPL resolution as the uniform linear array.

Figure 5.15 is the spectrum measured by the array with the driver at position 5 and the tunnel running at 81 ft/sec. At this tunnel velocity, the driver peak of 117 dB at 1000 Hz was approximately equal to the peak at 160 Hz produced by the flow. Due to the lack of velocity corrections in the beamforming algorithm, the DOA plot for the uniform linear array shown in Figure 5.16 (a) displays a peak of 132.6 dB at a look direction of 80° instead of the actual look direction of 65°. The resolution of the peak is about 0.6 dB. For subtracting the wind noise from the array spectrum, the uniform linear array produces an improved resolution of about 1.4 dB(Figure 5.16 (b)). From Figure 5.17 (a), it is observed that the MRA produces a peak of about 135 dB at a look direction of 80°. The resolution is approximately 0.8 dB. On subtracting the wind noise from the MRA spectrum, the resolution increases to about 3 dB with the DOA peak approximately at 120.5 dB as displayed in Figure 5.17 (b). The look direction of the peak for this plot remains at 80° as in Figure 5.17 (a).

A test was also carried out with the driver at position 5 driven at 1000 Hz, and the tunnel wind velocity at 151 ft/sec. At this velocity, the signal produced by the driver is completely buried in the wind noise, thus resulting in an extremely poor resolution of the DOA peak produced by the beamforming algorithm.

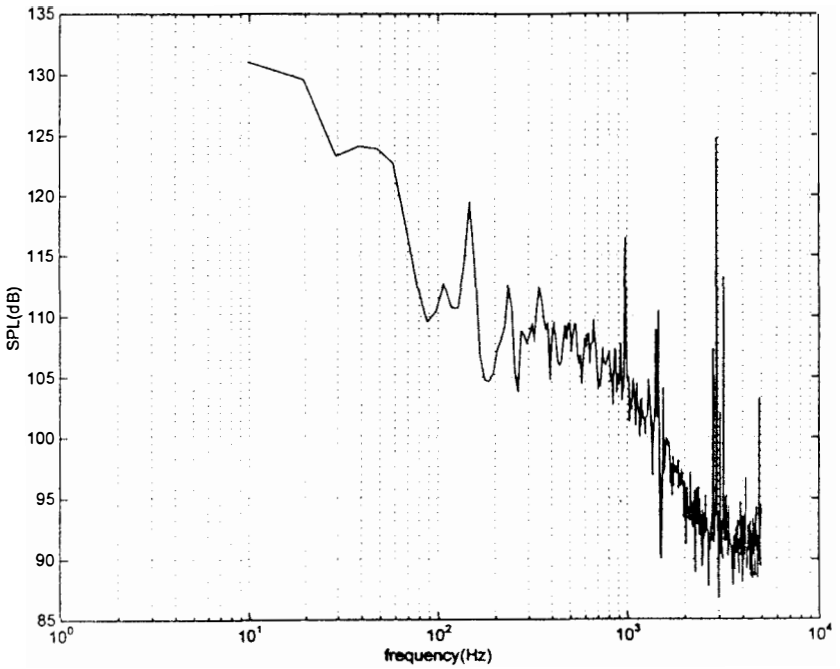

Figure 5.15 Spectrum of the Uniform Linear Array, Driver in Wind Tunnel at Position 5(65°), v = 81 ft/sec.

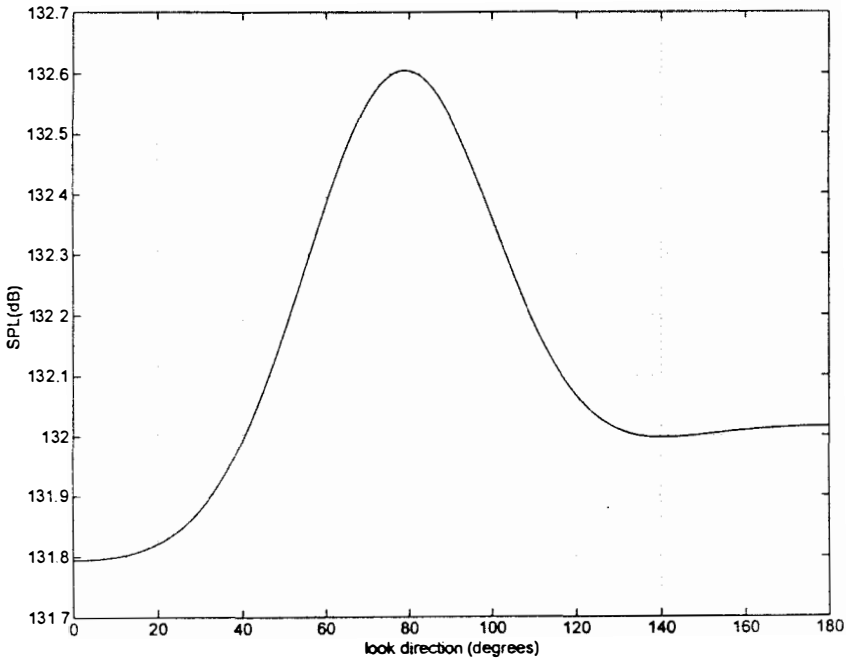

(a)

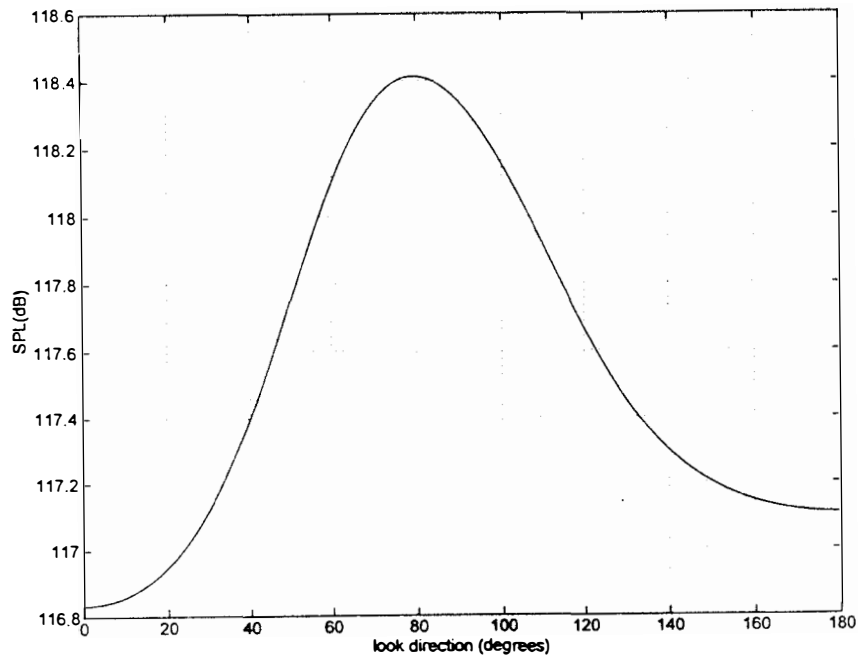

(b)

Figure 5.16 DOA Plot, Uniform Linear Array, Driver in Wind Tunnel at Position 5(65°), v = 81 ft/sec. (a) Wind Noise not Subtracted, (b) Wind Noise Subtracted.

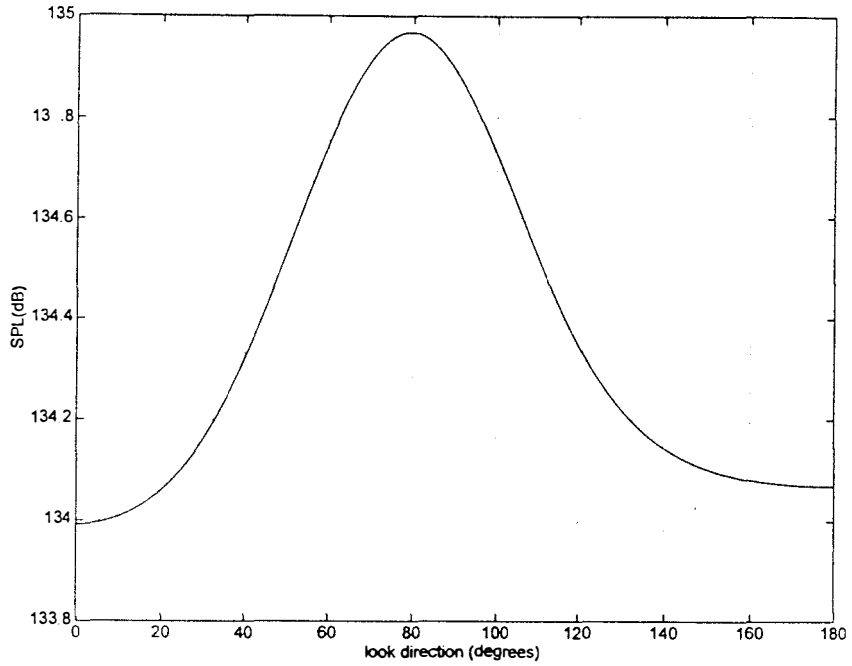

(a)

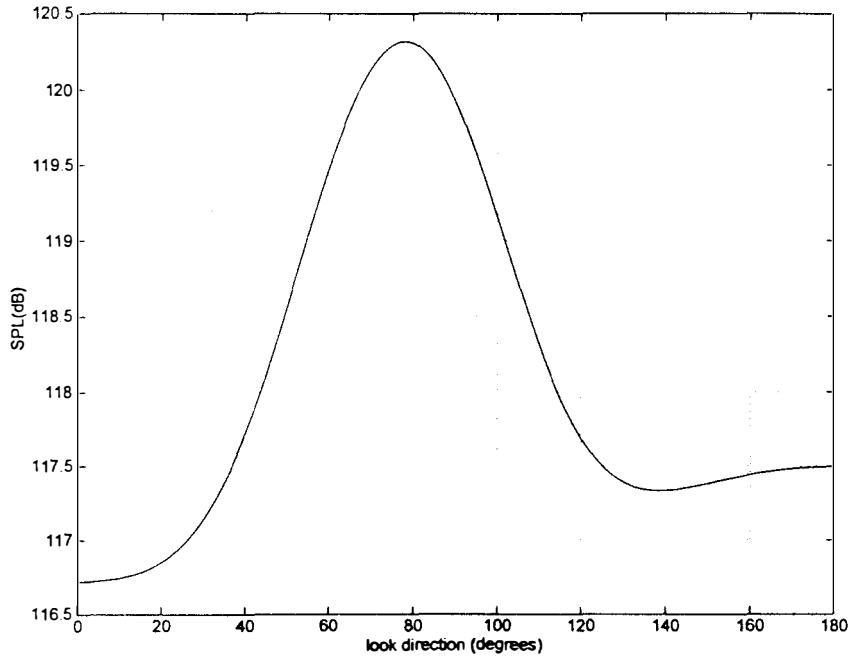

(b)

Figure 5.17 DOA Plot, MRA, Driver in Wind Tunnel at Position 5(65°), v = 81 ft/sec. (a) Wind Noise not Subtracted, (b) Wind Noise Subtracted.

Chapter 6

CONCLUSIONS AND FUTURE WORK

6.1 Conclusions

Beamforming acoustic array analysis technique applied to open field measurements results show that the two linear arrays (uniform linear array and the minimum redundancy array) are effective in measuring amplitude and direction of arrival of a sound source generated by a driver placed within the solid collection angle determined by the aperture of the array, and the distance of the driver from the array. Direction of arrival peaks measured by the two arrays were accurate to within 3° of the actual position of the driver. The minimum redundancy array proved more accurate than the uniform linear array in terms of resolution because of the minimum redundancy array`s increased effective aperture over the uniform linear array.

The empty wind tunnel results with no models installed showed that the wind tunnel did not have peaks near the frequencies at the driver generated peaks. When the driver was tested within the wind tunnel, the two linear arrays measured a higher sound pressure level than what they measured in the open field. This was due to the presence of reverberation inside the wind tunnel. Reverberation also reduced the resolution of the direction of arrival peak measured by the two arrays. It was observed that the array direction of arrival peaks were off by 5° to 15° when there is a flow in the tunnel.This

was assessed to be due to the absence of a velocity correction procedure in the beamforming algorithm and the presence of a multipath environment. Also, the resolution of the peaks decreased as compared with the no flow condition. The resolution could be improved by subtracting the wind noise from the array spectrum. However, for the case where the driver signal was completely buried within the wind noise, beamforming results did not produce a resolution high enough to distinguish the driver noise from the wind noise. This was naturally expected.

6.2 Future Work

Future work will be directed towards improving directional sensitivity and resolution of measured acoustic amplitude. Two dimensional multi-arm spiral arrays provide much better resolution and sidelobe rejection in both the elevation and azimuthal directions of a sound source. Also, the application of an adaptive beamforming algorithm instead of the conventional beamforming described in this work, would improve the resolution of the sound source DOA peaks.

REFERENCES

REFERENCES

1. Vakili, A. D., and Gauthier, C., "Control of Cavity Flow by Upstream Mass-Injection," Journal of Aircraft, Vol. 31, No. 1, 1994, pp. 169-174.

2. Piersol, A. G., "Use of Coherence and Phase Data Between Two Receivers in Evaluation of Noise Environments," Journal of Sound and Vibration (1978) **56**(2), pp. 215-228.

3. Chung, J. Y., " Rejection of Flow Noise using a Coherence Function Method," Journal of Acoustical Society of America, Vol. 62, No. 2, August 1977.

4. Wlezien, R. W., Spencer, S. A., and Grubb, J. P., "Comparison of Flow Quality in Subsonic Pressure Tunnels," AIAA paper 94-2503, June 1994.

5. Shivashankara, B. N., "High Bypass Ratio Engine Noise Component Separation by Coherence technique," AIAA paper 81-2054, Oct. 1981.

6. Parthasarathy, S. P., Cuffel, R. F., and Massier, P. F., "Separation of Core Noise and Jet Noise, AIAA paper 79-0589, March 1979.

7. Bendat, J. S., "Modern Analysis Procedures for Multiple Input/Output Problems," Journal of Acoustical Society of America, **68**(2), Aug. 1980.

8. Bendat, J. S., "System identification from Multiple Input/Output Data," Journal of Sound and Vibration (1976) **49**(3), pp. 293-308.

9. Howlett, J. T., "A Study of Partial Coherence for Identifying Interior Noise Sources and paths on general aviation Aircraft," NASA TM-80197, December 1979.

10. Chung, J. Y., Crocker, M. J., and Hamilton, J. F., "Measurement of Frequency Responses and the Multiple Coherence function of the Noise generation of a Diesel engine," Journal of the Acoustical Society of America, Vol. **58,** No. 3, pp. 635-642**,** Sept. 1975.

11. Koss, L. L., and Alfredson, R. J., "Identification of Transient Sound Sources on a Punch Press,", Journal of Sound and Vibration (1974) **34**(1), pp. 11-33.

12. Soderman, P. T., and Noble, S. C., "A Directional Microphone Array for Acoustic Studies of wind tunnel Models," AIAA paper 74-640, July 1974.

13. Grosche, F. -R., Stiewitt, H., and Binder, B., "Acoustic Wind Tunnel Measurements with a Highly Directional Microphone," AIAA paper 76-535, July 1976.

14. Billingsley, J., and Kinns, R., "The Acoustic Telescope," Journal of Sound and Vibration (1976) **48**(4), pp. 485-510.

15. Brooks, T. F., Marcolini, M. A., and Pope, D. S., "A Directional Array Approach for the Measurement of Rotor Noise Source Distributions with Controlled Spatial resolution," Journal of Sound and Vibration (1987) **112**(1), pp. 192-197.

16. Elias, G., "Noise Source Localization with Focussed Antenna for Reduction Purposes," Presented at the Science et Defence Conference, France, May 1990.

17. Gramann, R. A., and Mocio, J. W., "Aeroacoustic Measurements in Wind Tunnels using Adaptive Beamforming Methods," Journal of the Acoustical Society of America, Vol. 97, No. 6, pp. 3694-3701, June 1995.

18. Dougherty, R.P., and Underbrink, J. R., "Practical Considerations in Focussed Array Design for Passive Broadband Source Mapping Applications, The Pennsylvania State University, May 1995.

19. Herkes, W. H., and Stoker, R. W., "Wind Tunnel Measurements of the Airframe Noise of a High-Speed Civil Transport,", AIAA paper 98-0472, January 1998.

20. Humphreys, W. M. Jr., Brooks, T. F., Hunter, W. W. Jr., and Meadows, K. R., "Design and use of Microphone Directional Arrays for Aeroacoustic Measurements," AIAA paper 98-0471, January 1998.

21. Bai, M.R., and Lee J., "Industrial Noise Source Identification by Using an Acoustic Beamforming System," Journal of Vibration and Acoustics, Vol. 120, April 1998, pp. 426-433.

22. Bendat, J. S., and Piersol, A. G., "Random Data : Analysis and Measurement procedures," Wiley - Interscience, 1971.

23. Dodds, C.J., and Robson, J.D., "Partial Coherence in Multivariate Random Processes," Journal of Sound and Vibration (1975), **45**(2), pp. 243-249.

24. Johnson, D.H., and Dudgeon, D.E., "Array Signal Processing," Prentice Hall Signal Processing Series, 1993.

25. Haykin, S., "Advances in Array Signal Processing, Volume 3," 1993.

26. Vakili, A.D., and Radhakrishnan, S., "An Investigation of Cavity Noise and its Attenuation," Technical Report for Dornier GmbH, Germany, July 1998.

APPENDICES

Appendix A

SPIRAL ARRAY

A.1 Spiral Array Details

A logarithmic spiral is a natural curve defined by

$$r = r_0 \exp\left(\frac{\theta}{\tan\gamma}\right)$$

where r and θ are the radius and polar angle of any point on the curve, the constant γ is the spiral angle, and r_0 is the initial radius corresponding to $\theta = 0$. Distributing array microphones along a logarithmic spiral results in a design with no repetitions of the vector spacings between elements. This design is expected to give a much better sidelobe performance than either the regularly spaced linear array or the Minimum Redundancy Array . The polar coordinates of the microphones arranged in a single arm spiral is given in Table A.2. The array has an inner radius of 0.85 inches, an outer radius of 4.22 inches, and a spiral angle of 73°. The ten microphones were flush-mounted on a circular aluminum plate in a logarithmic spiral configuration as shown in A.3.

The spiral array was tested in the open field with the sound source at positions 1 through 5 as shown in Figure 4.9, producing sound at 1000 Hz. Due to insufficient number of microphones, and a single arm spiral configuration, the spiral array results did

not show a SPL resolution high enough to distinguish the sound source from the background noise.

A.2 Polar Coordinates of the Spiral Array Microphones

Microphone	Microphone Position	
	Angle (deg)	Radius (in)
1	0	0.85
2	30	0.99
3	60	1.40
4	90	1.60
5	120	1.70
6	150	2.20
7	180	2.60
8	210	3.00
9	240	3.50
10	270	4.22

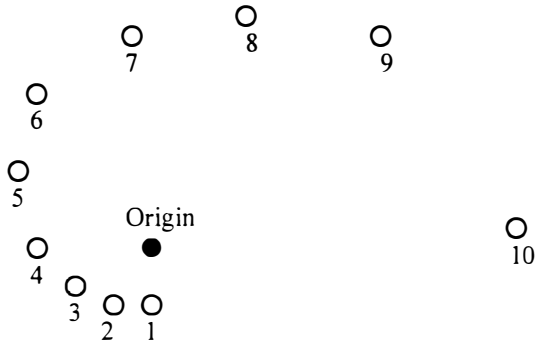

A.3 Ten Element Spiral Array Configuration

Appendix B

OPEN FIELD RESULTS

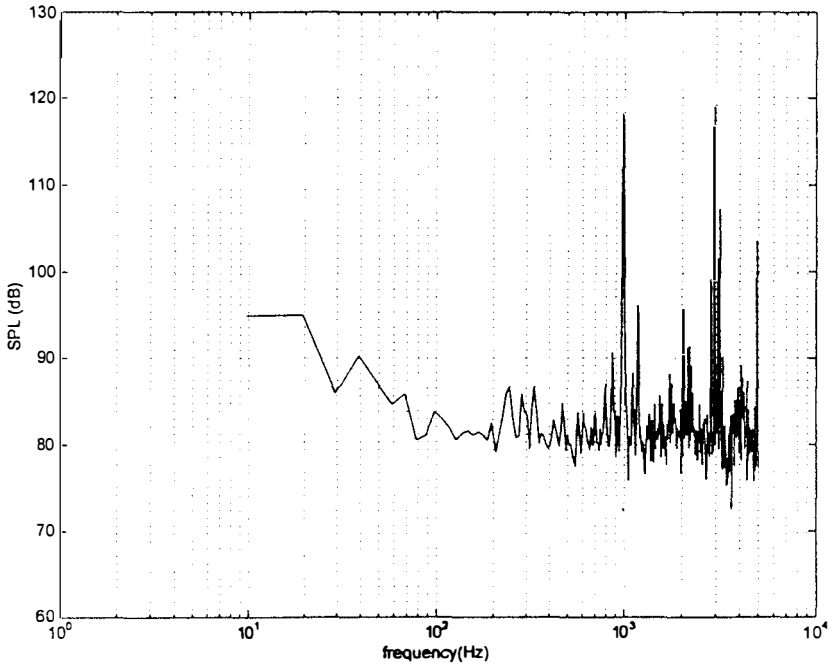

B.1 Spectrum of the Uniform Linear Array, Driver at Position 2 (95°), Open Field Test

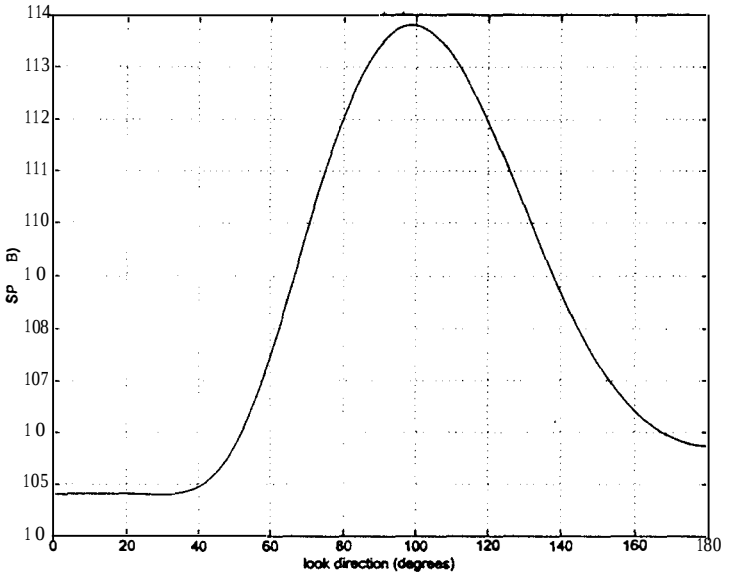

(a)

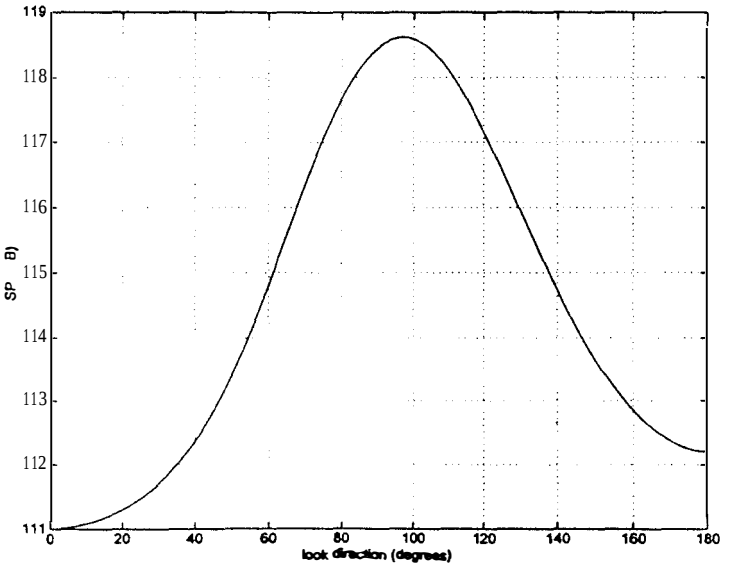

(b)

B.2 DOA plot for the (a) Uniform Linear Array, (b) MRA, Driver at Position 2 (95°) Open Field Test

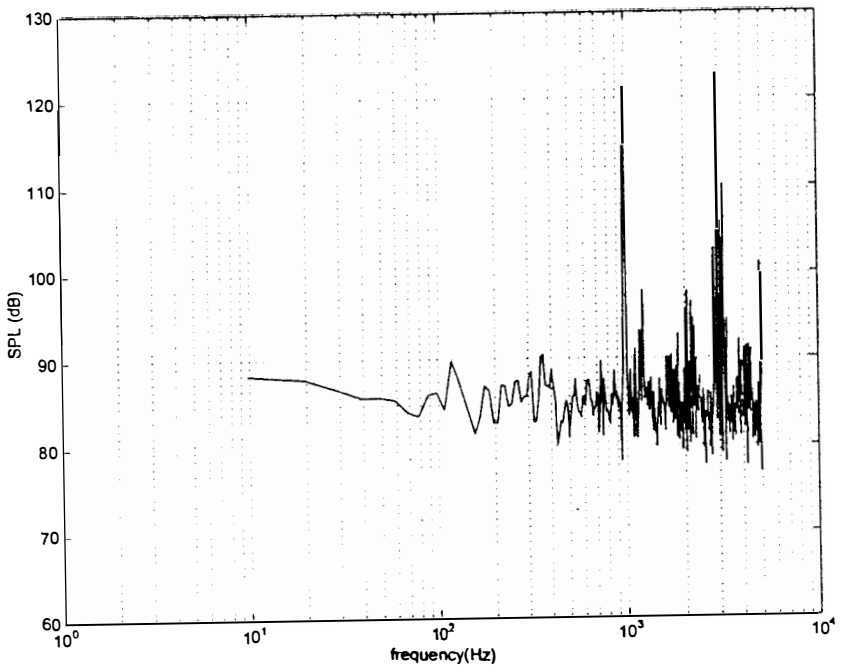

B.3 Spectrum of the Uniform Linear Array, Driver at Position 3 (85°), Open Field Test

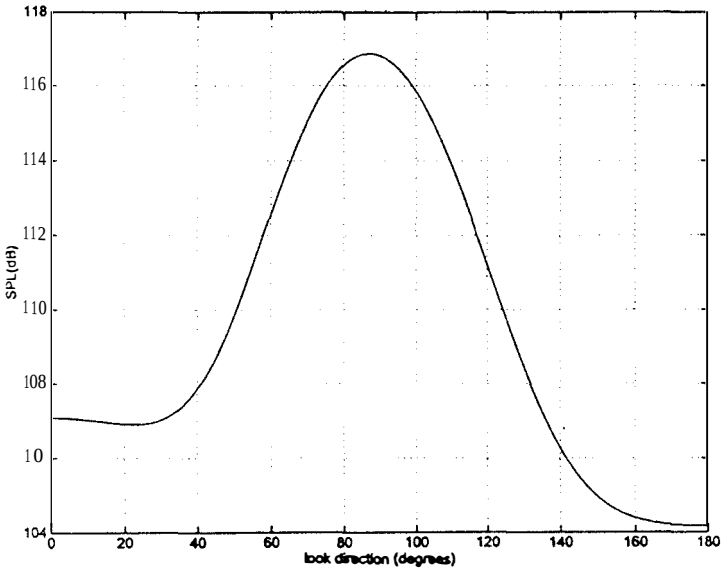

(a)

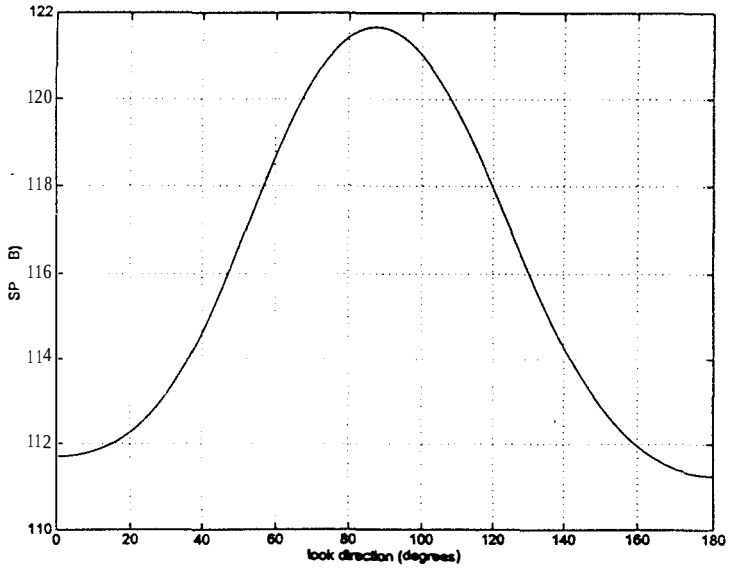

(b)

B.4 DOA plot for the (a) Uniform Linear Array, (b) MRA, Driver at Position 3 (85°) Open Field Test

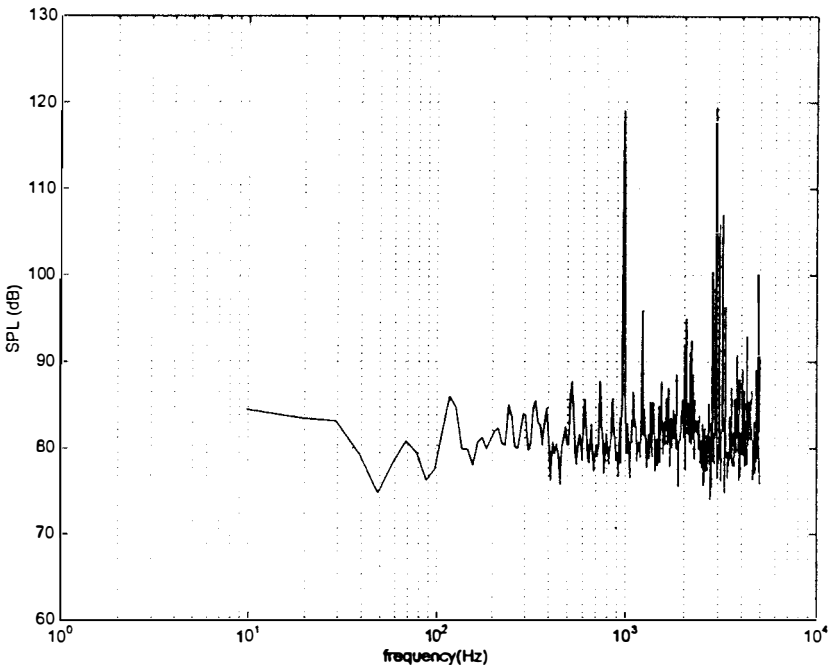

B.5 Spectrum of the Uniform Linear Array, Driver at Position 4 (75°), Open Field Test

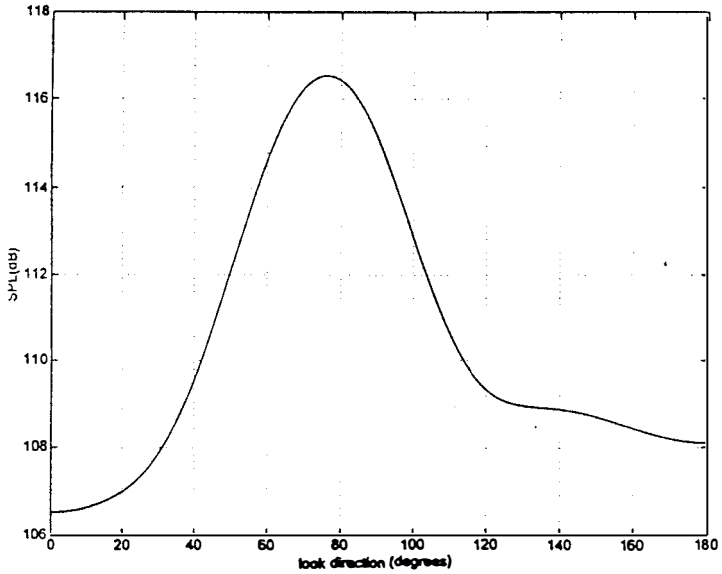

(a)

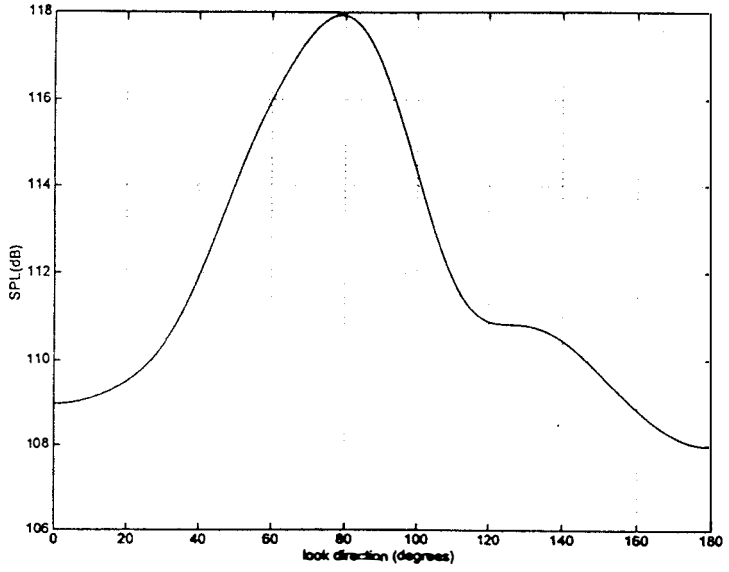

(b)

B.6 DOA plot for the (a) Uniform Linear Array, (b) MRA, Driver at Position 4 (75°), Open Field Test

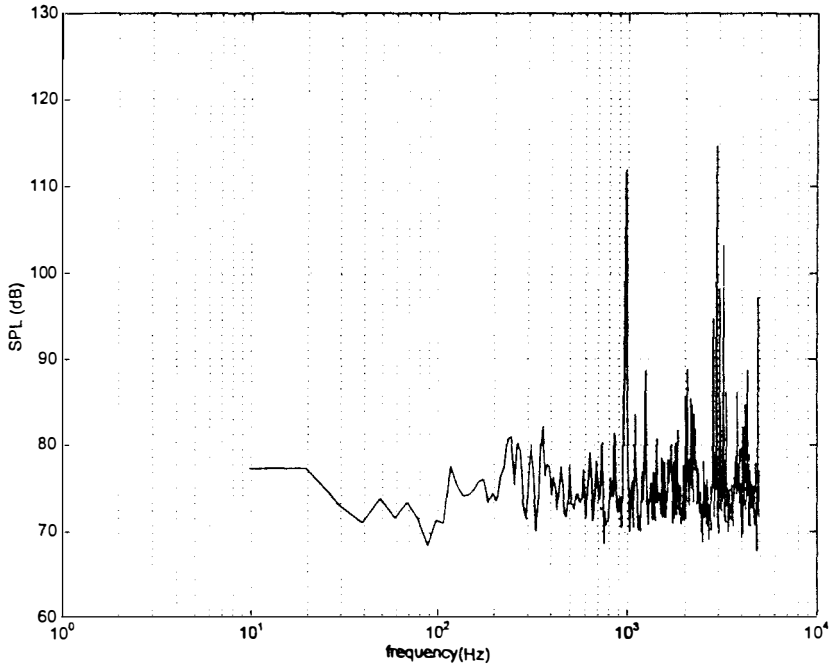

B.7 Spectrum of the Uniform Linear Array, Driver at Position 5 (65°), Open Field Test

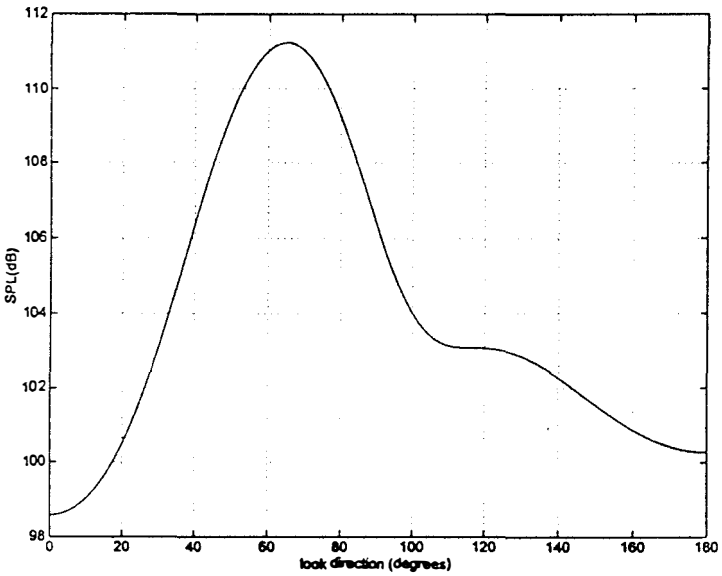

(a)

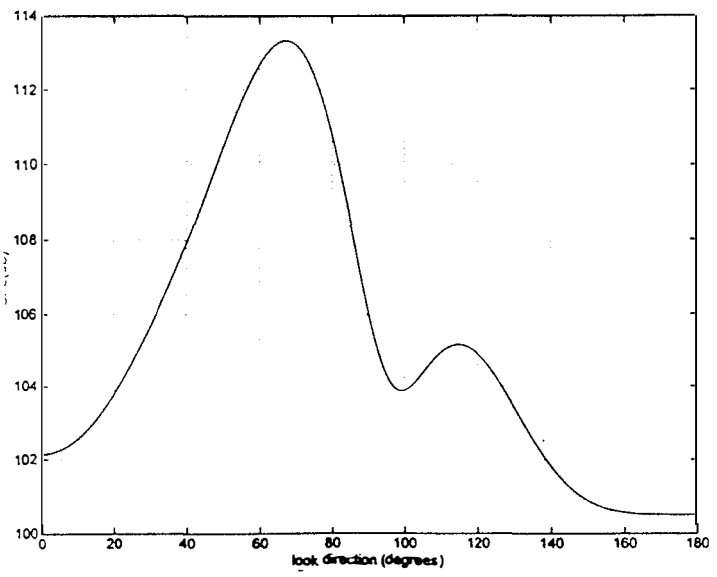

(b)

B.8 DOA plot for the (a) Uniform Linear Array, (b) MRA, Driver at Position 5 (65°), Open Field Test

VITA

Sekhar Radhakrishnan did his early schooling in various parts of India due to his father's itinerant career in the Indian Defense forces. Sekhar's fascination with flying led him to pursue a Bachelor's degree in Aeronautical Engineering at the Madras Institute of Technology. He finished his Master of Science in Aerospace Engineering at the University of Tennessee Space Institute in December 1998.